Comptes Rendus
Géoscience — Sciences de la Planète
2022, Vol. 354, Special Issue S2, p. 195-223
https://doi.org/10.5802/crgeos.155

The Mayotte seismo-volcanic crisis of 2018-2021 in the Comoros archipelago (Mozambique channel) / *La crise sismo-volcanique de 2018-2021 de Mayotte dans l'archipel des Comores (Canal du Mozambique)*

Temporal magmatic evolution of the Fani Maoré submarine eruption 50 km east of Mayotte revealed by in situ sampling and petrological monitoring

Évolution magmatique temporelle de l'éruption sous-marine de Fani Maoré, située à 50 km à l'est de Mayotte, révélée par un échantillonnage in situ et un suivi pétrologique

Carole Berthod[*, a, b], **Jean-Christophe Komorowski**[c], **Lucia Gurioli**[b], **Etienne Médard**[b], **Patrick Bachèlery**[b], **Pascale Besson**[c], **Pauline Verdurme**[b], **Oryaëlle Chevrel**[b], **Andrea Di Muro**[c, d], **Aline Peltier**[c, d], **Jean-Luc Devidal**[b], **Sophie Nowak**[c], **Isabelle Thinon**[e], **Pierre Burckel**[c], **Samia Hidalgo**[c], **Christine Deplus**[c], **Benoît Loubrieu**[f], **Delphine Pierre**[f], **Sylvain Bermell**[f], **Mathilde Pitel-Roudaut**[f], **Yvan Réaud**[g], **Sacha Fouchard**[g], **Manon Bickert**[h], **Anne Le Friant**[c], **Fabien Paquet**[e], **Nathalie Feuillet**[c], **Stephan L. Jorry**[f], **Yves Fouquet**[f], **Emmanuel Rinnert**[f], **Cécile Cathalot**[f] and **Elodie Lebas**[c]

[a] Université Clermont Auvergne, CNRS, IRD, OPGC, Laboratoire Magmas et Volcans, F-63000 Clermont-Ferrand, France

[b] SEDISOR; Univ. Brest UMR6538, IUEM, Plouzané, France

[c] Université de Paris, Institut de physique du globe de Paris, CNRS, F-75005 Paris, France

[d] Observatoire Volcanologique du Piton de la Fournaise, Institut de physique du globe de Paris, F-97418 La Plaine des Cafres, France

[e] BRGM-French Geological Survey, 3 avenue Claude Guillemin, BP36009, F-45060 Orléans Cédex 2, France

[f] Geo-Ocean, UMR 6538 Ifremer, Université de Bretagne Occidentale, CNRS, F-29280 Plouzané, France

[g] CNRS, Genavir, F-29280 Plouzané, France

[*] Corresponding author.

[h] Dipartimento di Scienze Chimiche e Geologiche, Università di Modena e Reggio Emilia, Modena, Italy

E-mails: berthod@ipgp.fr (C. Berthod), komorow@ipgp.fr (J.-C. Komorowski), lucia.gurioli@uca.fr (L. Gurioli), etienne.medard@uca.fr (E. Médard), Patrick.BACHELERY@uca.fr (P. Bachèlery), besson@ipgp.fr (P. Besson), pauline.verdurme@uca.fr (P. Verdurme), oryaelle.chevrel@uca.fr (M. O. Chevrel), dimuro@ipgp.fr (A. Di Muro), peltier@ipgp.fr (A. Peltier), J.L.Devidal@opgc.univ-bpclermont.fr (J.-L. Devidal), shidalgo@ipgp.fr (S. Nowak), i.thinon@brgm.fr (I. Thinon), burckel@ipgp.fr (P. Burckel), shidalgo@ipgp.fr (S. Hidalgo), deplus@ipgp.fr (C. Deplus), Benoit.Loubrieu@ifremer.fr (B. Loubrieu), Delphine.Pierre@ifremer.fr (D. Pierre), Sylvain.Bermell@ifremer.fr (S. Bermell), mathilde.pitel@ifremer.fr (M. Pitel-Roudaut), Yvan.Reaud@genavir.fr (Y. Réaud), Sacha.Fouchard@genavir.fr (S. Fouchard), mbickert@unimore.it (M. Bickert), lefriant@ipgp.fr (A. Le Friant), F.Paquet@brgm.fr (F. Paquet), feuillet@ipgp.fr (N. Feuillet), Stephan.Jorry@ifremer.fr (S. L. Jorry), Yves.Fouquet@ifremer.fr (Y. Fouquet), Emmanuel.Rinnert@ifremer.fr (E. Rinnert), cecile.cathalot@ifremer.fr (C. Cathalot), elebas@ipgp.fr (E. Lebas)

Abstract. The "Fani Maoré" eruption off the coasts of Mayotte has been intensively monitored by applying methods similar to those used for subaerial eruptions. Repeated high-resolution bathymetric surveys and dredging, coupled with petrological analyses of time-constrained samples, allowed tracking the evolution of magma over the whole submarine eruptive sequence. Indeed, after one year of direct ascent (Phase 1), basanitic magma switched to a different pathway that sampled a tephri-phonolitic subcrustal reservoir (Phase 2). Later, the magma pathway shifted again in the crust resulting in a new eruption site located 6 km northwest of the main edifice (Phase 3). The petrological signature of lava flows reveals both an evolution by fractional crystallization and syn-eruptive mixing with a tephri-phonolitic magma.

We demonstrate that high-flux eruption of large volumes of basanitic magma from a deep-seated reservoir can interact with shallower reservoirs and remobilize eruptible magma. This has significant hazards implications with respect to the capacity of such large eruptions to reactivate shallow-seated inactive reservoirs from a transcrustal magmatic system that could be located potentially at a distance from the high-flux eruptive site.

Résumé. L'éruption au large de Mayotte a été intensément surveillée en appliquant des méthodes similaires aux éruptions sub-aériennes. Une étude pétrologique et géochimique des échantillons dragués couplée à de nombreux relevés bathymétriques, nous a permis de suivre l'évolution du magma au cours de l'éruption. Le trajet du magma change après un an de remontée directe (Phase 1), un réservoir magmatique sous-crustal et plus différencié est alors échantillonné (Phase 2). Un mois plus tard, le trajet change à nouveau et engendre une migration du site éruptif à 6 km au nord-ouest de l'édifice principal (Phase 3). La signature pétrologique des coulées de lave révèle à la fois une évolution par cristallisation fractionnée et un mélange syn-eruptif avec un magma téphri-phonolitique. Nous démontrons qu'une éruption à haut débit impliquant de grands volumes de magma basanitique et provenant d'un réservoir profond peut interagir avec des réservoirs plus superficiels et remobiliser le magma éruptible. Ceci a des implications significatives en termes de risques quant à la capacité de ces grandes éruptions à réactiver des réservoirs inactifs peu profonds provenant d'un système magmatique transcrustal et potentiellement situé à distance du site éruptif.

Keywords. Fractional crystallization, Mixing, Mayotte, Submarine eruption, Dredging, Petrological monitoring, Magmatic system.

Mots-clés. Cristallisation fractionnée, Mélange, Mayotte, Éruption sous-marine, Dragage, Suivi pétrologique, Système magmatique.

Published online: 9 December 2022, Issue date: 17 January 2023

1. Introduction

Volcanic eruptions are monitored using various real-time methods, of which seismology, geodesy, and gas- and water-geochemistry are most commonly used to track magma migration through the Earth's crust. In recent years, with the evolution of sampling methods, and of chemical, petrological and textural

analysis techniques applied to solid volcanic products (pyroclasts and lavas), it has become more and more common to carry out near real-time petrological monitoring of eruptions [e.g., Liu et al., 2020, Re et al., 2021, Corsaro and Miraglia, 2022]. The analysis of lava and pyroclasts is carried out after volcanic eruption [Gurioli et al., 2005, Piochi et al., 2005, Di Muro et al., 2014] or occasionally during the eruption [Thivet et al., 2020]. Petrological and geochemical monitoring makes it possible to track the evolution of the magma bodies involved in an eruption, by following the variations in their physical and chemical parameters, such as crystal and gas content, or compositions of solid, liquid and gas phases. These data, when obtained within a short period (a few days to tens of days) after magma emplacement, can be combined with other real-time monitoring data to constrain the magma dynamics during an ongoing eruption. Linking deep magmatic processes to surface geophysical and geochemical records is not only an essential step in interpreting the precursor signals of eruptions but can also be crucial for understanding changes in the eruptive regime during the course of an eruption [Reubi et al., 2019, Gansecki et al., 2019, Bamber et al., 2020, Sundermeyer et al., 2020, Magee et al., 2021].

In contrast with subaerial eruptions, submarine eruptions are much more challenging to monitor. Indeed, their submarine context limits access to direct live observations of the volcanic activity. It is often impossible to know, even approximately, the timing of lava and/or pyroclasts emplacement and, hence, trace their temporal evolution [Resing et al., 2011, Casas et al., 2018, Carey et al., 2018, Clague et al., 2018]. Here, we present new petrological and geochemical evolution of the 2018–2021 submarine eruption that occurred off the eastern coast of Mayotte. This major eruption provided a unique opportunity to carry out frequent and targeted sampling of eruptive products whose emplacement date was constrained with repeated bathymetric surveys. In addition, one active incandescent submarine lava flow was sampled during a dredge (DR18). This sample collection permits constituting one of the most valuable petrological and geochemical databases for any known submarine eruption and particularly given that the eruption occurred at a depth between 2500 and 3500 m below sea level (BSL).

We first report an improved dredging protocol that allowed "surgical strikes" at >2500 m BSL to individually sample each eruptive unit of the newly emplaced volcanic material. Next, we provide a detailed petrological analysis of the most representative formations encountered among the sampled lavas. We use these data to constrain the eruptive history of the Fani Maoré volcanic edifice, taking into account the timing of the lava emplacement, and tracking the magma pathway through the crust.

2. Geological setting

Mayotte is the easternmost island of the Comoros Archipelago located in the Mozambique Channel between the eastern coast of Mozambique and the northern tip of Madagascar. This archipelago is composed of four main islands, namely from east to west Mayotte, Anjouan, Moheli, and Grande Comore, which are associated with atolls and partially emerged reef platforms and interconnected by a series of submarine volcanic chains [Tzevahirtzian et al., 2021, Thinon et al., 2022]. The Comoros Archipelago is characterized by active volcanism and tectonics associated with an area of active seismicity that connects the northern extremity of Madagascar in the east to the African coast in the west. This volcanic chain is interpreted as the NW–SE boundary between the Lwandle microplate and the Somalia plate, on the periphery of the East African Rift System [Bertil and Regnoult, 1998, Famin et al., 2020, Feuillet et al., 2021, Thinon et al., 2022] or as a zone of broad deformation extending up to the northern half of Madagascar [Stamps et al., 2021].

Recent volcanic activity has been recorded on Grande Comore [Karthala and La Grille volcanoes, Bachèlery et al., 2016], Anjouan [Quidelleur et al., 2022], and Mayotte [Feuillet et al., 2021]. Karthala Volcano (Grande Comore Island) is one of the largest active volcanoes in the world and the second most active volcano in the Indian Ocean with four eruptions from 2005 to 2007 [Bachèlery et al., 2016, Morin et al., 2016, Thivet et al., 2022]. New K–Ar and ^{14}C ages demonstrate that volcanism is still active on Anjouan, with the youngest activity around 9.6 ka [Quidelleur et al., 2022]. Finally, despite Mayotte being the oldest island of the archipelago with

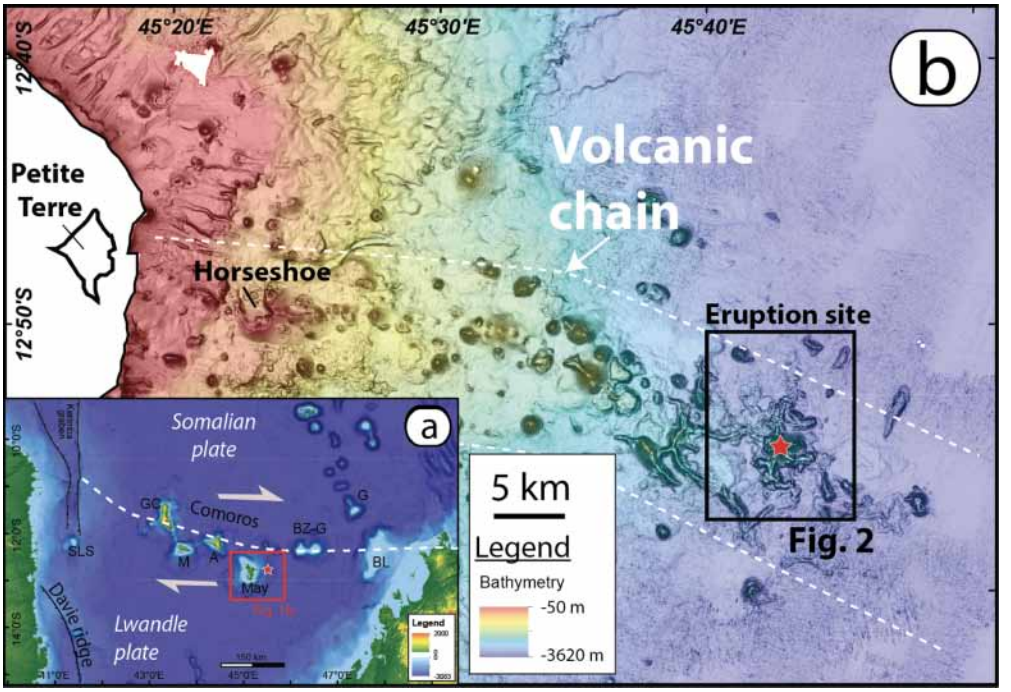

Figure 1. Location of the eruptive site off Mayotte's coast. (a) Comoros Archipelago, underlining the NW–SE boundary between the Lwandle microplate and the Somalia plate from Famin et al. [2020] (white dashed line), is composed of two emerged banks (Zelée and Geyser banks) four main volcanic islands, from east to west, Mayotte (May), Anjouan (A), Moheli (M) and Grande Comore (GC). Red star: eruptive site, G: Glorieuses; BL: Leven Bank; SLS: St Lazarus Seamount. (b) Fani Maoré volcanic cone is located 50 km east from offshore Mayotte Island, at the end of the Eastern Volcanic Chain, as delineated by the white dashed lines [Bachèlery et al., 2021, Feuillet et al., 2021].

a maximum age of 28 Ma for the onset of magmatic activity [Masquelet et al., 2022], recent volcanic activity has been documented both on land [possibly as young as 4 ka, Zinke et al., 2003] and on the distal part of a 60 km long WNW–ESE-oriented volcanic chain that extends 50 km off the eastern submarine flank of Mayotte up to the 2018–2021 Fani Maoré new edifice [Figure 1; Berthod et al., 2021b, Feuillet et al., 2021]. Petite Terre, the eastern volcanic island of Mayotte, is characterized by the presence of recent volcanic activity [200 ka, Pelleter et al., 2014] ranging from older mafic Strombolian scoria cones to the younger well-preserved phonolitic tuff rings aligned on N140 trending fractures.

3. Eruption phenomenology

The 2018–2021 volcanic activity most likely started in early July 2018 after two months of intense seismic activity at mantle level [Cesca et al., 2020, Lemoine et al., 2020, Bertil et al., 2021], near the eastern end of what is now called the "Eastern Volcanic Chain of Mayotte" [Bachèlery et al., 2021, Feuillet et al., 2021]. When the new volcanic edifice, Fani Maoré was first discovered in May 2019, it had already grown to more than 820 m high above the seafloor, with an estimated lava volume of 5 km^3 [Feuillet et al., 2021]. This activity caused a strong mobilization of the French scientific community and the creation of the Mayotte Volcanological and Seismological Monitoring Network [REVOSIMA, 2022] to record seismic and track volcanic activity on Mayotte and thereby provide a better definition of the seismic and volcanic hazards on the island of Mayotte and along the active submarine volcanic chain. In response to this crisis, twenty-six oceanographic campaigns have been carried out since May 2019, six of them deploying rock

Table 1. Location of dredges performed during MAYOBS and GEOFLAMME oceanographic campaigns

Dredges	Oceanographic cruise	DOI https://doi.org/10.18142/291	Start dredging			End dredging		
			Latitude	Longitude	Depth (m)	Latitude	Longitude	Depth (m)
DR01	MAYOBS 1	https://doi.org/10.17600/18001217	12°54.30′ S	45°43.13′ E	3050	12°54.51′ S	45°43.08′ E	2820
DR08	MAYOBS 2	https://doi.org/10.17600/18001222	12°56.46′ S	45°42.88′ E	3072	12°56.05′ S	45°41.91′ E	3050
DR10	MAYOBS 4	https://doi.org/10.17600/18001238	12°54.94′ S	45°43.31′ E	3120	12°55.05′ S	45°43.24′ E	2950
DR11	MAYOBS 4	https://doi.org/10.17600/18001238	12°54.80′ S	45°41.57′ E	3250	12°55.20′ S	45°41.55′ E	3228
DR12	MAYOBS 4	https://doi.org/10.17600/18001238	12°52.90′ S	45°42.94′ E	3245	12°52.97′ S	45°42.93′ E	3200
DR14	MAYOBS 15	https://doi.org/10.17600/18001745	12°51.94′ S	45°40.65′ E	3240	12°51.94′ S	45°40.71′ E	3210
DR15	MAYOBS 15	https://doi.org/10.17600/18001745	12°52.71′ S	45°40.34′ E	3130	12°52.80′ S	45°40.49′ E	3070
DR18	MAYOBS 15	https://doi.org/10.17600/18001745	12°52.26′ S	45°41.17′ E	3270	12°52.27′ S	45°41.03′ E	3265
DR19	GEOFLAMME	https://doi.org/10.17600/18001297	12°50.63′ S	45°40.96′ E	3363	12°50.92′ S	45°40.81′ E	3369
DR20	GEOFLAMME	https://doi.org/10.17600/18001297	12°52.09′ S	45°40.35′ E	3224	12°52.24′ S	45°40.23′ E	3135

dredges [Feuillet, 2019, Feuillet et al., 2021, Fouquet and Feuillet, 2019, Jorry, 2019, Rinnert et al., 2020, 2021]. These campaigns involve seven multiparameter volcano monitoring cruises [Feuillet, 2019, Fouquet and Feuillet, 2019, Jorry, 2019, Rinnert et al., 2020, 2021], three scientific research campaigns, GEOFLAMME [Rinnert et al., 2021], SISMAORE [Thinon et al., 2021], and SCRATCH [Berthod et al., 2021c], as well as sixteen short campaigns to retrieve and redeploy OBSs (Ocean Bottom Seismometers) every 3–4 months since February 2019.

These campaigns provide an exceptional time-series of bathymetric, textural, petrological, and geochemical data for the 2018–2021 eruptive period (Table 1). Indeed, repeated, high-resolution bathymetric surveys, coupled with dredging of erupted lava at intervals ranging from few hours to few months, allowed us to follow the syn-eruptive evolution of the magma throughout the last two years, until the probable end of the eruption in January 2021 when the last active lava flows were detected.

Using data collected during these oceanographic campaigns, recent studies suggest that the 2018–2021 eruption has been fed by a deep magmatic system rooted in the lithospheric mantle [e.g., Berthod et al., 2021b, Feuillet et al., 2021, Foix et al., 2021, Lavayssiere et al., 2022]. Using dredged volcanic rocks gathered during the first three monitoring campaigns [MAYOBS 1, 2, and 4, Feuillet, 2019, Jorry, 2019, Fouquet and Feuillet, 2019, Rinnert et al., 2019], Berthod et al. [2021b] concluded that primary magma is extracted from the mantle at depths of 80–100 km before being stored in a deep magma reservoir inside the lithospheric mantle. Petrological [Berthod et al., 2021b] and seismic [Feuillet et al., 2021, Foix et al., 2021, Lavayssiere et al., 2022] data indicate that the depth of this reservoir is ≥35 km and probably less than 48 km. After ~50% of crystallization in this deep reservoir, and extremely efficient segregation from its cumulates, an internal or external trigger forced the magma to ascend directly and quickly to the surface where it erupted as aphanitic basanites [Berthod et al., 2021b] from the onset of the eruption (May 2018 to May 2019). After May 2019, the magma output rate slowed down and switched to a different ascent pathway sampling a small shallower evolved magma batch at the base of the crust at a depth of 18 ± 9 km [Berthod et al., 2021a].

4. Methods

4.1. *Dredging protocol*

Despite considerable improvements in navigation and sampling methods in the last decades, including the development of Remotely Operated Vehicles (ROV) and human operated submersibles (e.g., the manned submarine *Nautile*), dredging operations remain fundamental for sampling and characterizing submarine volcanic structures and related products. Its strength relies on its capability to collect a large quantity of material (up to 1000 kg) that can be used for various analyses and can usually be regarded as statistically representative of the studied area. Since dredging requires fewer logistics than submersibles,

the related operations are easier to implement, and were, until the late 1960s, the only way to sample the seabed [Kidd et al., 1990]. In recent decades, significant advances have included more accurate navigation systems, improved geophysical survey methods, and monitoring dredge behavior to ensure that dredge sampling is as representative as possible of the geological terrains being investigated. By contrast, the design of the dredge used for geological purposes has remained very simple due to the high risk of equipment breaking during the operation. R/V (Research Vessel) *Marion Dufresne II* and R/V *Pourquoi Pas?* use a cylindrical dredge made of a cylindrical metal base, cut into a 1 m diameter steel pipe with cutting teeth welded at the edge in order to break off samples from outcrops. The dredge is linked to the oceanographic winch cable through swivels, 25 m of cargo ship mooring chain and 150 m of martyr cable. A fuse link is also inserted between the metal bail and the chain connection to ensure the rupture of the martyr cable above a threshold tension of 120–160 kN. Indeed, if the dredge hooks on an outcrop and remains stuck, the increasing tension places the ship's trawl warp at risk of parting. An ultra-short baseline (USBL) acoustic beacon (BUC) is positioned on the trawl cable at about 365 m from the dredge, in order to record the precise 3D location of the dredge during the entire operation.

4.1.1. *Preparation*

An improved preparation procedure was adopted to select the location and the topographic profile to be dredged. Several elements had to be considered beforehand to select the most optimal dredging profile within the studied area:

- For active volcanoes such as Fani Maoré, a bathymetry differential using the ship's multibeam echosounder allowed us to pinpoint potential new eruptive products (such as lava flows). In some cases, bathymetry was acquired by ROV or AUV (Autonomous Underwater Vehicle) with a higher resolution. In addition, if available, the geological map, slope angles and the reflectivity maps were used to better define the sampling area.
- For dredging to be effective, we preferred to operate on a smooth slope (from base to top without major breaks in slope) so that, the dredge would be properly orientated and could easily grab material without emptying on hooking. However, on some occasions, dredges were also successfully performed on nearly flat profiles, where a difference in elevation of only a few meters existed.
- Accounting for meteorological conditions was also critical, and the vessel was aligned as much as possible with the currents and wind directions and preferably facing the wind and the current, so as to simplify the ship's maneuvers during dredging. Note that meteorological conditions could change quickly and on occasions the approach had to be adjusted once the vessel arrived on site. For better efficiency, several topographic profiles with different orientations were prepared in advance using GIS software to quickly adapt the course of the ship if needed.
- The general start and end of the sampling zone of interest was fixed according to the geological and bathymetric information available. The ship's captain could thus plan the location of the entire dredging operation according to the conditions at the time. This requires a precise knowledge of the bathymetry not just in the zone of interest of dredging, but on a longer track that is usually about 7 km.
- The dredge was carefully cleaned to ensure that no rock fragments were retained in the metal mesh. We occasionally attached below the cylindrical dredge a "*baby-dredge*" which consists of a heavy and resistant iron cast tube about 0.5 m long and 20 cm in diameter that hangs with a solid chain below the main dredge in order to sample the finer grained material forming the seabed that easily gets lost filtering through the 3–5 cm sized openings in the metal mesh of the main dredge. This turned out to be extremely useful on submarine pyroclastic cones as it allowed us to sample the pyroclastic matrix of unconsolidated volcanic deposits from submarine explosive activity.

The geographical coordinates of the dredging profile (latitude, longitude, and depth) were then

extracted with the help of GIS software (ESRI® ArcGIS or QGIS) to plot the depth profile versus decimal minutes of longitude or latitude at a 1:1 scale. This graph was then used to report the GPS coordinates of the USBL acoustic beacon to track the position of the dredge graphically precisely during the entire process.

4.1.2. *Dredging*

The dredge was launched at the beginning of the profile and deployed by unwinding the cable at a speed of 1 m/s. When the dredge reached the seabed, the vessel started to move towards the end point of the profile at about 0.5 m/s (1 knot) and the cable deployment speed was reduced to about 0.3 m/s. The goal of this step was to tilt the dredge cable line to form an angle of about 40° with the seafloor and to increase the efficiency of dredging. During our campaigns, about 4100 m of cable were deployed for dredging operations at around 3500 m water depth.

Once the optimum tilt was reached, the cable deployment was stopped, the ship slowed down to 0.25 m/s (0.5 knots) and the dredging operation started following the dredge route planned previously. All the information, from the descent to the end of the dredging operation, was recorded. A tensiometer monitored the load on the ship's cable to follow the dredge behavior on the seabed, and to identify potential "hooks" when the dredge was supposedly sampling. For each hook, we recorded on the dredge profile (i) the position of the BUC, (ii) the time, and (iii) the tension of the cable. The known length between the BUC and the dredge (e.g., 365 m during MAYOBS 15 campaign) allowed us to precisely locate the dredge on the seafloor on a 2D plot of the dredge profile. For the latest MAYOBS 21 campaign, dredging was also followed with the software *VGraph3D* in which the topography is shown together with the position of the BUC and the vessel. Careful attention was paid to the time-series of the hooks along the dredging profile to interpret in real-time the behavior of the dredge, whether it was stuck, and whether it had lifted off the seabed, potentially empty. The amplitude of the hooks was carefully monitored so that they do not exceed the 120-kN safety threshold. After half a dozen hooks, the vessel stopped and the hopefully full dredge was brought back on board and its weight recorded. While pulling the dredge, several new hooks were often recorded that might have caused the dredge to get stuck. When this happened, we often managed to free the dredge by driving the vessel backward until it was in vertical alignment with the dredge so that the cable could be rewound a bit thus lifting the dredge off the blockage point.

For sampling sites located at 3500 m BSL, the entire dredging operation usually lasted approximately 6 h: 1.5 h for launching and descent at 1 m/s, 1.5 h for deployment, 1 h for dredging, and 1.5 h for ascent and boarding.

4.2. *Chemical analyses*

4.2.1. *X-ray fluorescence analyses (XRF)*

Bulk-rock major element compositions were obtained for forty-seven samples from ten dredges on the eruption site (Table 1). Samples were analyzed with an Epsilon 3 × l X-ray fluorometer (Malvern-Panalytical) at the plateforme "Rayons X"—Université de Paris (Paris, France). The fluorometer is equipped with an Ag X-ray tube operating under He atmosphere, with four conditions during 120 s: 5 kV–60 μA without filter for analysis of Na, Mg, Al and Si, 10 kV–30 μA with a 7 μm titanium filter for the analysis of P, 12 kV–25 μA with a 50 μm aluminum filter for the analysis of Ca, K and Ti, and 20 kV–15 μA with a 200 μm aluminum filter for analysis of Mn and Fe. Samples were mixed with a fluxing agent (0.1136 g of sample, 1.2312 g of fluxing agent, either $LiBO_2$ or $Li_2B_4O_7$) and 0.0187 g of non-wetting agent (LiBr) and melted in a platinum crucible at 1050 °C for 25 min in a fusion instrument (LeNeo fluxer, Claisse). Calibration curves were obtained from identical beads of fifteen geological reference materials (ACE, ANG, BCR-2, BEN, BHVO-2, BIR-1, BXN, DTN, FKN, GSN, MAN, Mica-Fe, Osh BO, UBN and BR24). The curves are perfectly linear over the entire concentration range. Analytical uncertainties ($\pm 1\sigma$) are <5% for TiO_2, MnO and Fe_2O_3; 5% for MgO, SiO_2 and CaO; 10% for Al_2O_3, P_2O_5 and K_2O and 20% for Na_2O.

4.2.2. *ICP-MS analyses*

Trace element concentrations were analyzed by ICP-MS at Institut de Physique du Globe de Paris (IPGP, Paris, France). Around 50 mg of powdered rock

samples were digested using a mix of 2 ml concentrated HNO_3 and 1 ml concentrated HF, heated in closed Teflon vessels at 110 °C for 24 h. An additional 3 ml of concentrated HNO_3 was added to the samples after cooling and the mix was heated for another 24 h at 110 °C. Finally, 45 ml of ultrapure water was added to the samples after cooling and the solutions were sonicated for 4 h. Samples were analyzed 24–48 h later, after an additional 10× dilution with ultrapure water, using an inert introduction system on an Agilent 7900 ICP-MS. Calibration of rock samples was done against a BEN rock standard [Jochum et al., 2016]. Analytical uncertainties are 6% or less for lithophile elements and 15% or less for chalcophile elements.

4.2.3. *Electron probe microanalysis*

The chemical composition of minerals and glasses was analyzed using the CAMECA SXFive Tactis electron microprobe at Laboratoire Magmas et Volcans (LMV, Clermont-Ferrand, France). For minerals, we used a 15 kV accelerating potential and a 15 nA probe current with a focused beam for major and minor elements, with 10 s counting times. We analyzed both mineral rims and cores although no difference was visible except for olivine antecrysts. For glasses, the beam current was reduced to 8 nA, the beam was defocused to a 20 μm diameter, and alkali elements were counted first in order to avoid Na loss caused by beam interaction. Glasses were only analyzed in glassy areas close to pillow rims and away from crystals to avoid any modification due to diffusion during quenching. Natural and synthetic mineral standards, including orthoclase (K, Al), albite (Na), wollastonite (Si, Ca), fayalite (Fe), forsterite (Mg), $TiMnO_3$ (Ti, Mn), NiO (Ni), Cr_2O_3 (Cr), and fluorapatite (P) were used for routine calibration.

5. Results

5.1. *Lava flows chronology*

Repeated bathymetric surveys with the ship's multibeam echosounder have systematically been gathered during the MAYOBS campaigns over the areas of eruptive activity following specific data acquisition protocols, leading to bathymetric grids with a resolution of 7 m to 30 m. Some of the key objectives of these repeated surveys were to be able to track the evolution of the active lava flow field along with the eruptive activity. Due to the depth of the volcano, new volcanic materials can be inferred when depth changes between two surveys exceed 10 m over a sufficiently large area. In some conditions, this depth differential threshold can be as low as 5 m. After each survey, a preliminary analysis of depth differences was achieved, and the results announced by the REVOSIMA. A re-examination of the whole bathymetry dataset is now in progress to quantify more accurately the volumes and flux of erupted material and their evolution over time.

Figure 2 synthesizes the spatio-temporal evolution of the overall contours of the different active lava flows. The compound lava flow field was mapped after each bathymetric survey using a combination of bathymetric data, differential time-lapse bathymetric analysis and ocean bottom reflectivity data. Several phases of lava flow eruption can be identified, ordered chronologically, and matched with the corresponding dredges performed during the different surveys (Figure 2). Phase 1 corresponds to the volcanic field and the new edifice discovered during the first MAYOBS campaign [Feuillet et al., 2021]. The structure, evidenced by comparing their data to those acquired during a 2014 survey by the French Naval Hydrographic and Oceanographic Service (SHOM), is composed of a main central edifice with radial ridges, up to 300 m thick and extending up to 5 km north and south, emplaced between July 2018 and May 2019 [Figure 2a, Feuillet et al., 2021]. Phase 2 marks the emplacement, from new vents, of two widespread lava flow fields in the southern and southwestern distal part of the main edifice. Between August 2019 and January 2021, numerous lava flows were emplaced in a new distinct area, located 6 km northwest from the main central edifice suggesting the occurrence of a third phase (Figure 2a,b). The growth of the main edifice stopped sometime between August 2019 and May 2020. At the time of writing (June 2022), preliminary estimates indicate that the entire eruption produced a bulk volume (not corrected for vesicularity) of about 6.55 km^3 of magma [Deplus et al., 2019, REVOSIMA, 2022]. The eruptive flux was very high during Phase 1, on the order of 150 to 200 m^3/s [REVOSIMA, 2019, Deplus et al., 2019] and progressively decreased throughout the eruption (Phase 2) and in particular for lavas emplaced at the northwestern site, during Phase 3 [Berthod et al., 2021b, REVOSIMA, 2020].

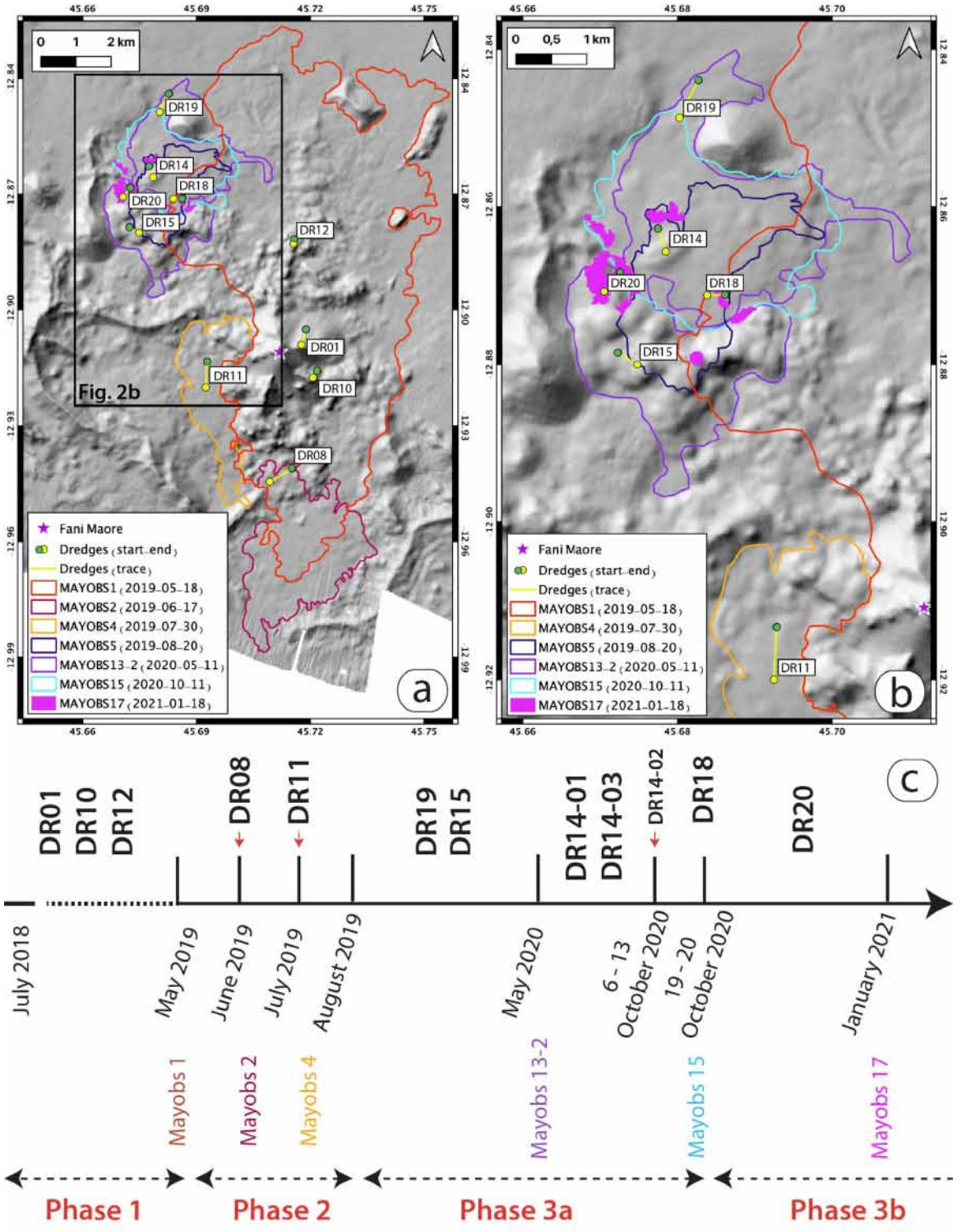

Figure 2. Caption continued on next page.

Figure 2. (**cont**.) (a) Distinct lava flows identified from bathymetry data collected during the MAYOBS oceanographic campaigns [Feuillet, 2019, Jorry, 2019, Fouquet and Feuillet, 2019, Rinnert et al., 2019] and the GEOFLAMME cruise [Rinnert et al., 2021]. DR labels correspond to the dredges. (b) Close-up view on the last eruptive site, located 6 km northwest of the main volcanic cone and collected during the MAYOBS 15 campaign [Rinnert et al., 2019] and the GEOFLAMME campaign [Rinnert et al., 2021]. (c) Sampling related to eruption timing. DR01, DR10 and DR12 lavas were erupted before May 2019 during the cone-building (Phase 1); DR08 and DR11 are lava flows erupted in June and July 2019 (Phase 2). DR14-01/03 sampled a lava flow erupted between May and October 2020, while DR15 and DR19 sampled different facies of a complex lava flow field erupted between August 2019 and May 2020 (Phase 3a). DR14-02 lava was erupted between the October 6th–13th 2020 and DR18 sampled a lava flow erupted on the night of October 19th–20th 2020 and which has been observed glowing red with the SCAMPI camera during MAYOBS 15 campaign [REVOSIMA, 2020, Rinnert et al., 2020], DR20 erupted between 20 October 2020 and 18 January 2021 (Phase 3b). The subdivision of Phase 3 is proposed from our petrological observations. See Section 5.3 for further explanation.

5.2. *Samples*

Most dredged samples are fragments of pillow lavas, centimetric to pluridecimetric in size (Figure 3a), that present five different textural facies that are described as follows from the outside to the inside.

Facies 1 is the quenched, shiny glassy black outer rim with a thickness of about 2–3 cm thick (Figure 3b). This chilled margin, of variable thickness, is cracked and micro-vesiculated. It flakes off easily, sometimes very dynamically as a popping rock, forming numerous glass fragments. The vesicle's concave outer surfaces are often coated with golden metallic deposits giving a very distinctive iridescent sheen to the glassy lava. When preserved, the surface of this facies is wrinkled with millimetric grooves. This surface is often covered with clusters of orange precipitates, which can also fill fractures within the pillow.

Facies 2 is thicker (6–7 cm), less glassy with a less shiny and duller appearance compared to Facies 1. Although it is massive, it is nevertheless characterized by an increase in the size and proportion of vesicles (Figure 3b). The vesicles are mostly sub-spherical with diameters varying between 3.5 mm to 2.0 cm. However, the convoluted shape and irregular outline of the largest vesicles are evidence that coalescence is observable and tends to increase towards the internal part of the pillow lava. All thin sections were made in the outermost chilled margin preserved in the recovered clasts (mostly Facies 1, exceptionally Facies 2) to ensure a rapid quenching in contact with water, and to avoid post-eruptive crystallization processes.

Facies 3 is characterized by the presence of many centimeters long (4–5 cm), tubular but undulating pipes that are oriented perpendicular to the quenched pillow outer surface and that do not penetrate through the lower contact with Facies 2 (Figure 3b).

Facies 4 is characterized by elongated vesicles parallel to the boundary between Facies 3 and Facies 4 (Figure 3b). This part of the pillow is also characterized by prismatic fractures forming a polygonal pattern.

Finally, Facies 5 corresponds to the core of the pillow lava. It often shows a succession of centimetric layers sub-parallel to the outer glassy surface (Facies 1) that are characterized each by a homogeneous vesicularity that differs from the next neighboring layer which can be more vesiculated, in terms of vesicle size and abundance. Vesicles tend to be aligned along a direction sub-parallel to the outer glassy convex surface of the pillow. Vesicles have coalesced to form cavities (2 × 3 cm in size) that have joined together to form radial pipes that are generally perpendicular to the outer pillow's surface (Figure 3b).

5.3. *Petrology*

5.3.1. *Phase 1: lavas of the main edifice*

Samples from Phase 1 (DR01, DR10, and DR12) are glassy, almost aphyric [<4 vol.% crystals, Berthod et al., 2021b] and highly vesicular (average vesicularity of 35 vol.%). Crystals include 50–700 μm olivine co-crystallizing with smaller 50–100 μm magnetite

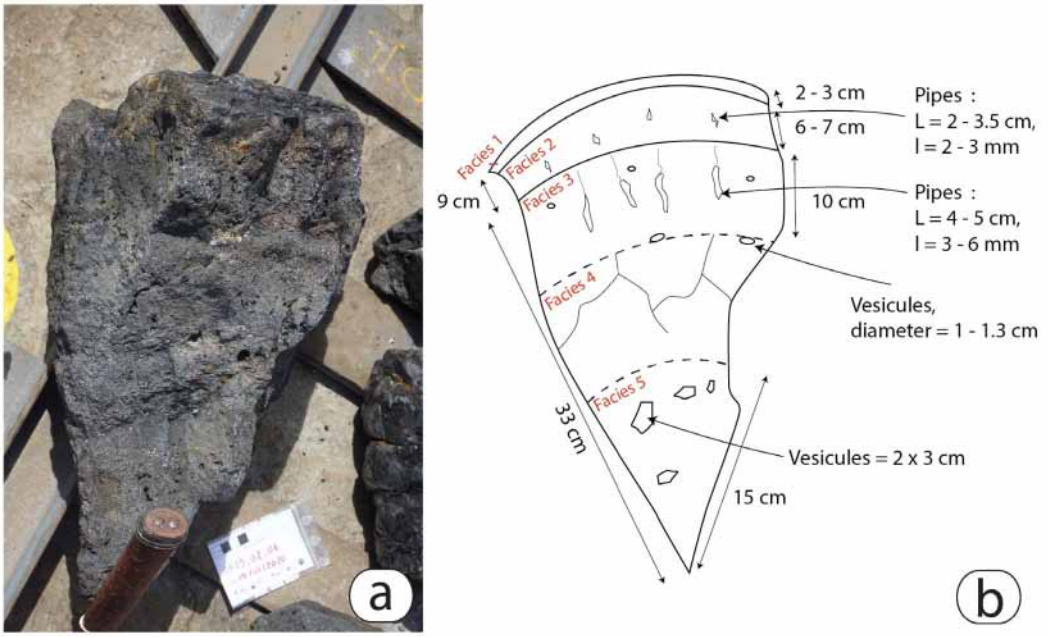

Figure 3. (a) Picture and (b) simplified sketch of a poorly fractured pillow-lava dredged during the MAYOBS campaigns (DR15-02), measuring 42 × 39 × 36 cm.

(Figure 4a,b), often grouped as small clusters. Many olivine crystals are skeletal, with numerous inclusions and embayments, although euhedral crystals are also present. Most magnetite crystals display euhedral shapes. Olivine and magnetite crystals are observed in the chilled margins. No apatite or ilmenite have been observed.

5.3.2. *Phase 2: distal lavas from the southern and southwestern eruptive vents*

Samples from Phase 2 (DR08 and DR11) display glassy and aphyric textures (Figure 4c,d). Clusters of olivine and magnetite crystals, similar to those observed in Phase 1 samples, are here associated with apatite crystals (up to 20 μm in length). The textural relationships suggest that all three minerals crystallized at the same time. The formation of an early immiscible sulfide melt is evidenced by the presence of small spherical droplets of iron sulfide (<10 μm in diameter).

A small number of large (up to 2.5 mm long) reversely zoned olivine crystals with Fe-rich cores and Mg-rich overgrowths are present in all samples from Phase 2. Since Berthod et al. [2021a] showed that these crystals were sampled by the basanitic magma during its ascent towards the surface, they are interpreted as antecrysts. Some of the cores contain numerous embayments. Contrary to the outer euhedral faces, these embayments do not display overgrowths (Figure 4e). Co-crystallization of magnetite with olivine, as observed within Phase 1 samples, is also found in the Mg-rich overgrowth. Rounded ilmenite grains, surrounded by magnetite overgrowths, are observed in all samples (Figure 4f). Ilmenite inclusions, associated with magnetite and apatite, are observed in some olivine Fe-rich cores. Rare millimetric antecrysts of clinopyroxene and rounded apatite crystals have been described in one sample [Berthod et al., 2021b].

5.3.3. *Phase 3a: northwestern eruptive area*

After August 2019, the activity shifted to a new eruptive area 6 km northwest of the main edifice (Figure 2a,b). The petrological description of lava flows from this Phase 3 are presented chronologically (Figures 5 and 6).

The first erupted lava flows at the northwestern site (DR15 and DR19) show a similar mineralogy than Phase 2 samples. They contain clusters of euhedral to skeletal olivine crystals (50 to 500 μm, Figure 5a,b),

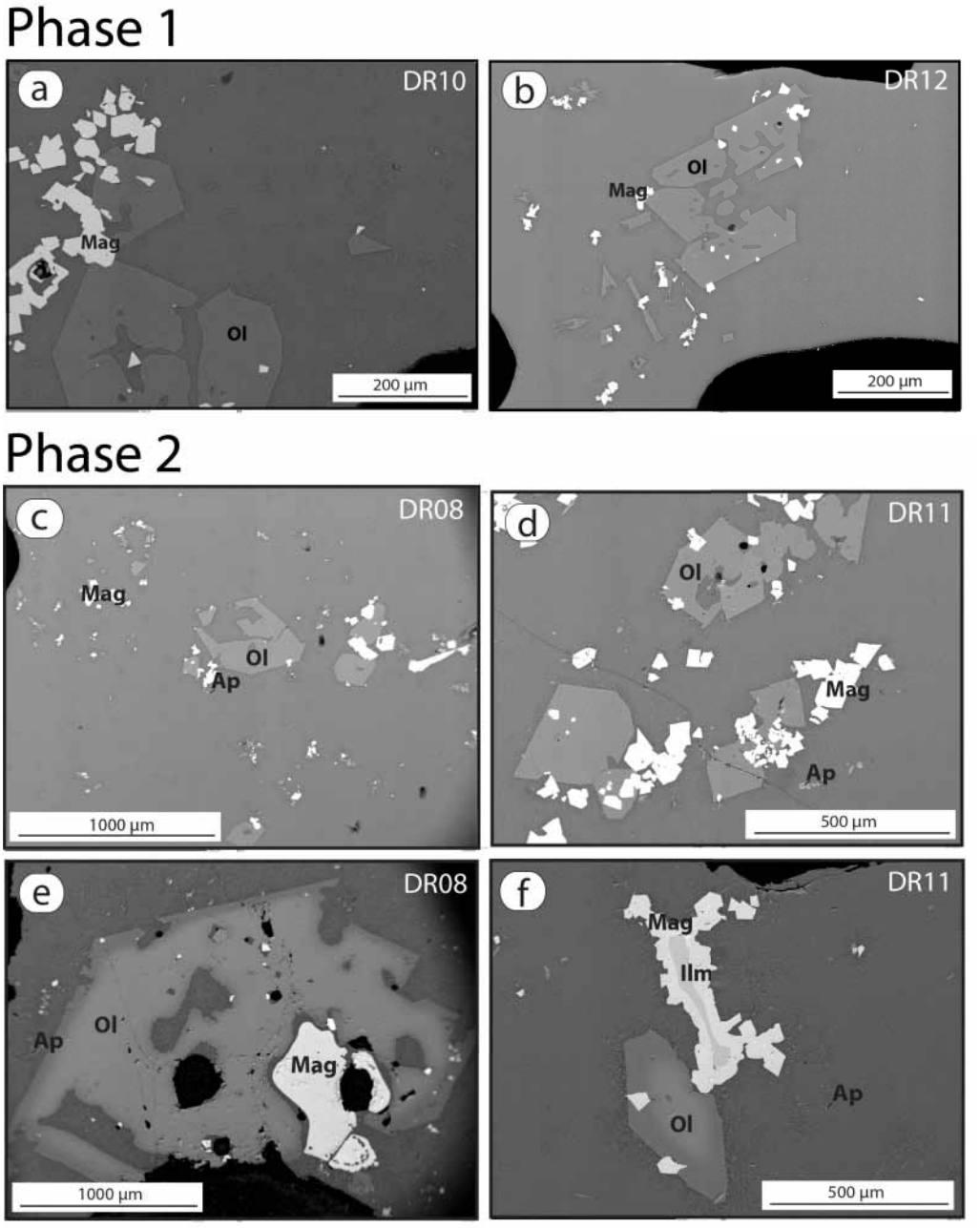

Figure 4. Back-scattered electron (BSE) microscope images of samples from Phases 1 and 2, (a) DR10 sample contains clusters made of co-crystallized skeletal olivine and euhedral magnetite crystals. Skeletal olivine in intergrowth with magnetite are also observed in (b) DR12, (c) DR08, and (d) DR11 samples. Apatite crystals also appear in these Phase 2 samples. Reversely zoned olivine with rounded cores and rounded magnetite crystals are present in (e) DR08 and (f) DR11 samples. These Phase 2 lava flows also contain resorbed ilmenite surrounded by magnetite. Ol: Olivine, Mag: Ti-rich Magnetite, Ilm: Ilmenite, Ap: Apatite.

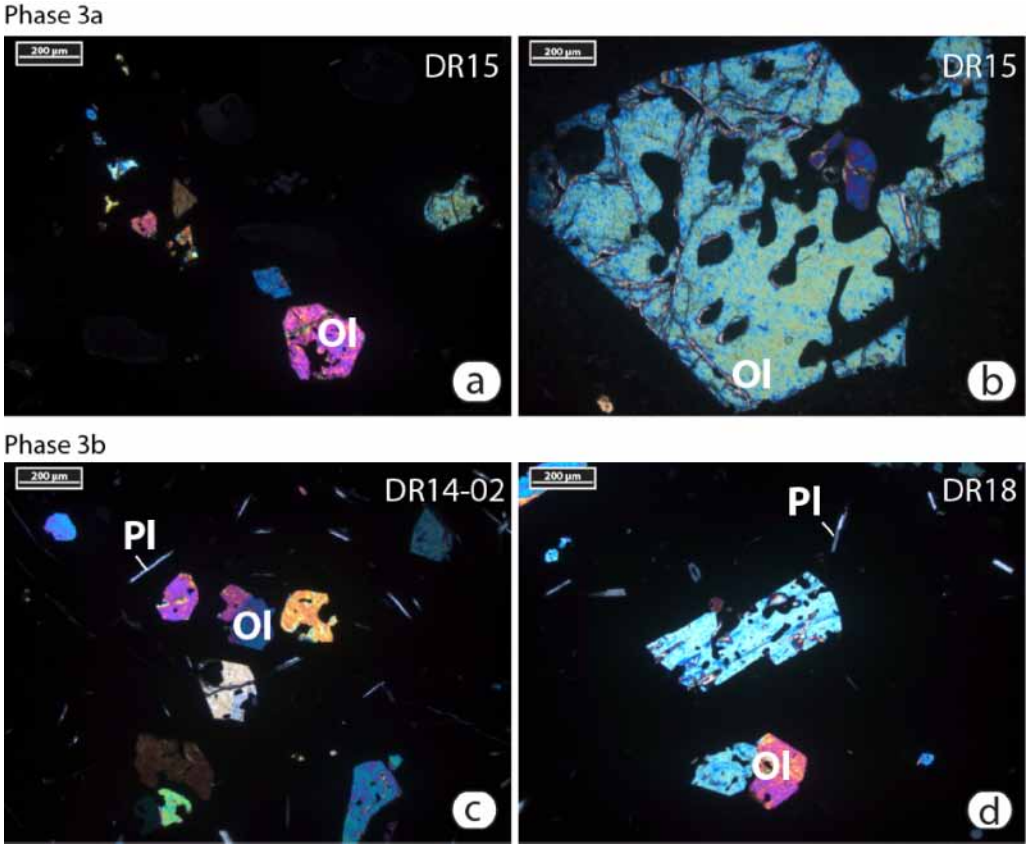

Figure 5. Petrographic characteristics of Phase 3 samples from the NW eruptive site viewed under cross-polarized transmitted light (a) typical olivine crystals in sample DR15. (b) Zoned olivine antecryst in sample DR15 with possible dissolution texture. (c) Sample DR14-02 and (d) sample DR18-01 contain plagioclase laths in the matrix. Ol: olivine, Pl: Plagioclase.

in intergrowth with magnetite (up to 200 µm) and apatite crystals. Euhedral to skeletal apatite crystals are more abundant than in Phase 2 samples and can reach 150 µm in length. Droplets of immiscible sulfide melts, up to 20–30 µm in diameter, are associated with or included in magnetite crystals. As with the Phase 2 lavas, those samples also contain an antecryst cargo comprising reversely zoned olivine (0.5–3 mm, Figure 5b) and rounded ilmenite crystals with magnetite rims (up to 800 µm, Figure 6a). No clinopyroxene has been observed.

Three different types of samples were recovered from dredge DR14: (i) samples labeled DR14-03 and DR15 are petrographically identical. (ii) Samples DR14-01 are also similar to DR15 but for the appearance of a few small plagioclase laths (Figure 6b). (iii) The third category of samples, DR14-02 is significantly different from the other DR14 samples and will be described below with the latest eruptive products.

5.3.4. *Phase 3b: most recent eruptive products*

The samples from the most recent lava flows (DR18-01, DR20, and DR14-02) from the NW eruptive area are glassy and contain crystals of olivine (<1000 µm), magnetite (<400 µm), apatite (<200 µm), and plagioclase (<500 µm, average 150 µm, Figures 5c,d and 6c,d). Olivine crystals are often skeletal and contain numerous melt inclusions and embayments. Olivine, apatite, and magnetite crystals show evidence of co-crystallization, whereas plagioclase crystals are isolated. The plagioclase content quickly increases toward the core

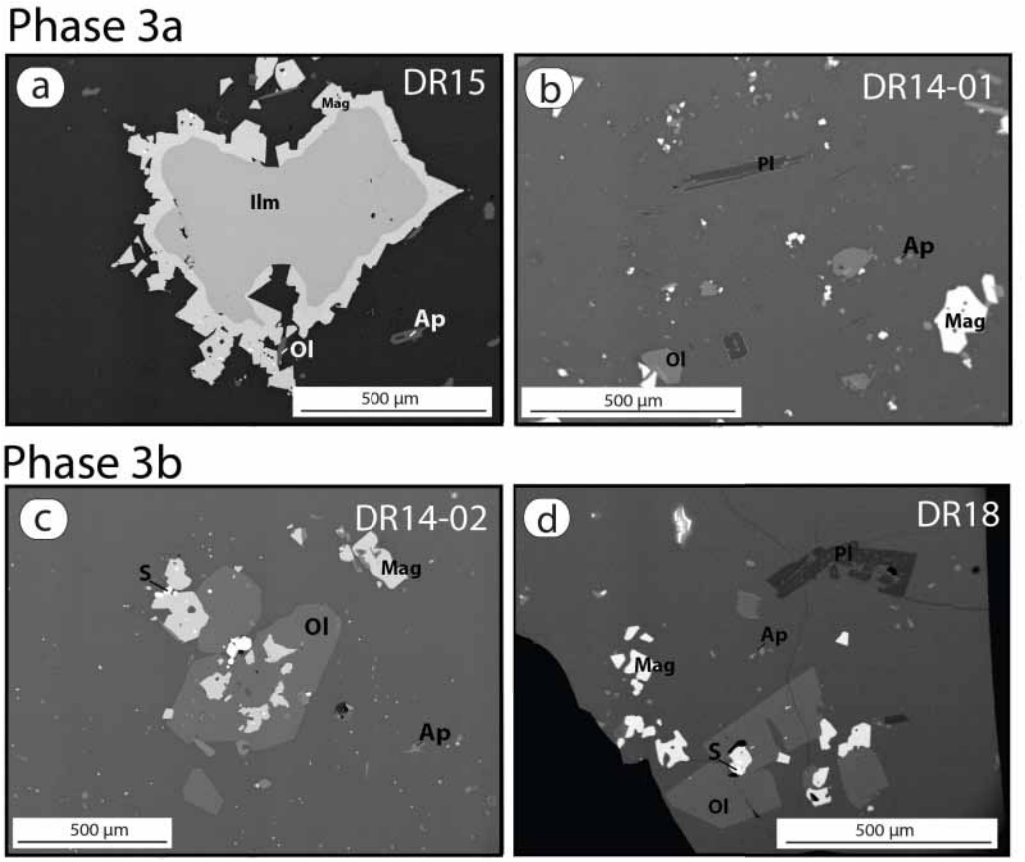

Figure 6. Back-scattered electron microscope images of Phase 3 samples from the Phase 3b, on north-western site. (a) Rounded ilmenite antecryst surrounded by magnetite in sample DR15. (b) Crystals of olivine, plagioclase, magnetite, and apatite in sample DR14-01. (c) Olivine-magnetite-sulfide cluster in sample DR14-02 (sulfide are the small light blebs inside the olivine and the larger one in-between the two largest olivine crystals). (d) Olivine, magnetite, plagioclase, and apatite crystals in sample DR18-01. Ol: Olivine, Mag: Ti-rich Magnetite, Ilm: Ilmenite, Ap: Apatite, S: Sulfide blebs.

of the pillow lava fragments, giving them a diktytaxitic texture. Contrary to DR15, DR19, and Phase 2 samples, no reversely zoned olivine or magnetite-rimmed ilmenite have been observed in those samples. Rounded sulfide droplets (up to 100 µm in diameter) are abundant, either as inclusions within oxides and sometimes within olivine, or associated with magnetite-olivine-apatite clusters.

The differences in paragenesis (absence/presence of reversely zoned olivine or magnetite-rimmed ilmenite, and plagioclase) and in droplet contents suggest that Phase 3 can be divided into two sub-phases: Phase 3a (DR14-01, DR14-03, DR15, and DR19) and Phase 3b (DR14-02, DR18-01, and DR20).

5.4. *Bulk-rock composition*

All major element data presented here (Figure 7 and Supplementary Table 1) have been normalized to 100%, volatile-free, to facilitate comparisons. Original XRF totals are reported in Supplementary Table 1. Major and trace element compositions are similar to those previously reported for the entire Comoros Archipelago [Späth et al., 1996, Claude-Ivanaj et al., 1998, Class et al., 1998, Deniel, 1998, Bachèlery and Hémond, 2016].

Overall, all erupted samples display a well-defined differentiation trend in all Harker-type element plots (Figure 7). The few outliers are likely due to some

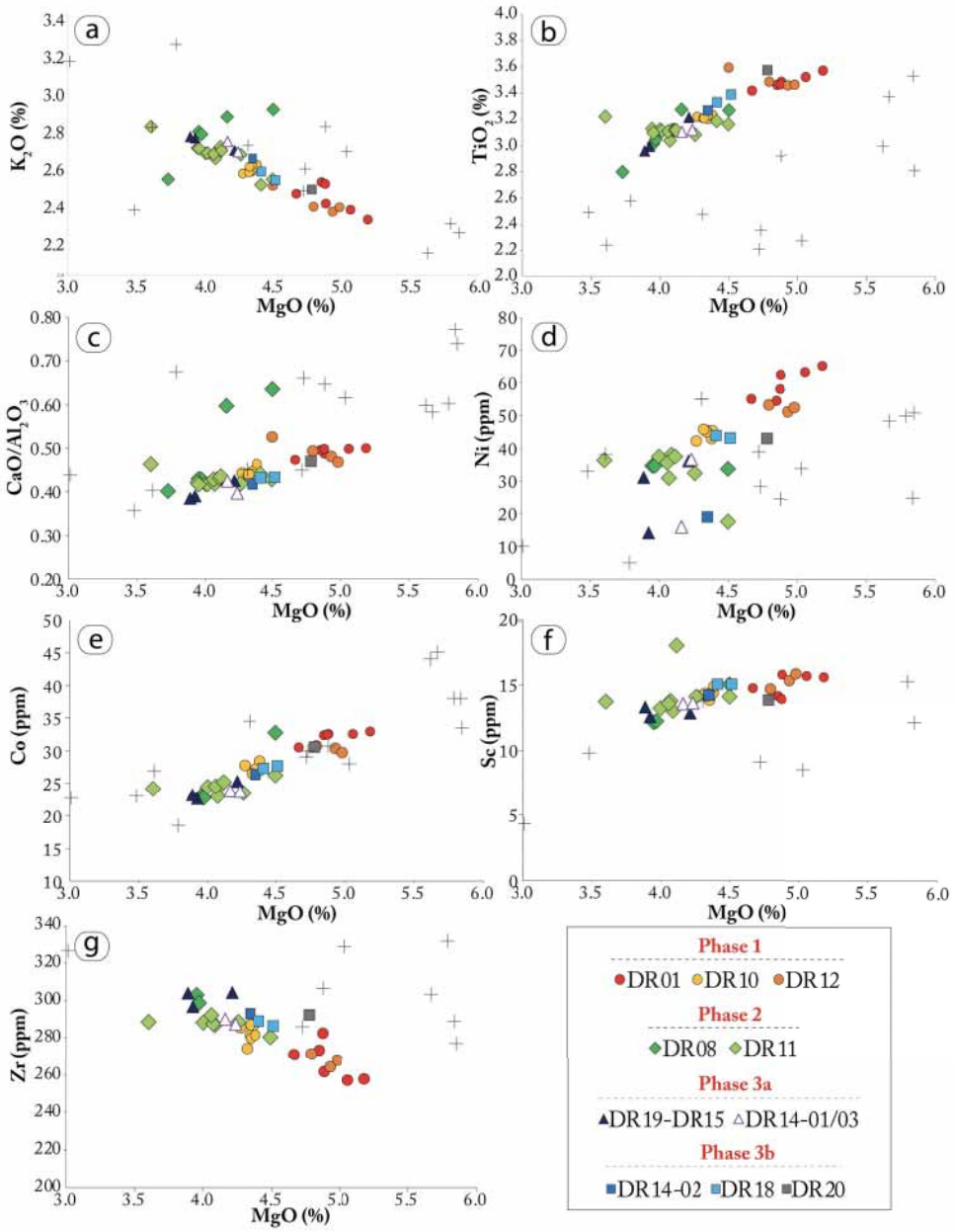

Figure 7. Bulk-rock geochemical evolution of dredged lavas from the eruption site. The caption presents dredges in chronological order. Crosses are reference data for Mayotte lavas [Nougier et al., 1986, Späth et al., 1996, Pelleter et al., 2014].

crystal accumulation. The most primitive samples are those erupted during Phase 1 (particularly samples from DR01), the most evolved samples have erupted either during Phase 2 (DR08 and DR11) or at the northwestern eruptive site during Phase 3 (DR15 and DR19).

Early erupted lavas of Phase 1 (DR01, DR10, and DR12) are evolved basanites with a MgO content of 4.0–5.0 wt% and a K_2O content of 2.2–2.5 wt% (Figure 7a,b). In these samples, TiO_2, Ni, Co, Sc and Zr contents vary from 3.0–3.4 wt%, 42.3–65.2 ppm, 26.5–32.9 ppm, 0.8–15.9 ppm, and 257–287 ppm

respectively (Figure 7c–g). Few variations are observed within the eruptive products of Phase 1, although DR01 is slightly more primitive than DR12 and DR10 with MgO ranging between 4.4–5.0 wt%, 4.3–4.7 wt%, and 4.0–4.2 wt%, respectively. K_2O, TiO_2, and Ni contents confirm this observation. Phase 2 lavas, sampled by DR08 and DR11 dredges, display more evolved basanitic compositions with 3.4–4.3 wt% MgO and 2.5–3.0 wt% K_2O. TiO_2 and Ni contents range from 2.4 to 3.1 wt% and 17.7 to 38 wt%, respectively. Co and Sc ranging from 22.8 to 32.8 ppm and from 12.1 to 18.0 ppm, respectively (Figure 7e,f).

The geochemical evolution of the eruptive products tends to continue for Phase 3a lavas on the new northwestern eruptive site (Figure 2a,b), with DR15 and DR19 characterized by the lowest MgO contents (3.6–4.0 wt%). TiO_2, Ni, Co, Sc and Zr contents are also slightly lower with values below 3.0 wt%, 36.2 ppm, 25.3 ppm, 13.3 ppm, and 305 ppm, respectively. K_2O content is above 2.5 wt%. Lavas from dredge DR15 are in the phono-tephrite field of a TAS diagram, not the basanite field. In contrast, all other samples still qualify as basanites.

Different types of samples are present within the DR14 dredge (Phase 3). DR14-01 and DR14-03 samples are similar to Phase 2 lavas with 3.8–4.1 wt% MgO, 2.5–2.6 wt% K_2O, 2.9–3.0 wt% TiO_2, 16.0–36.7 ppm Ni, 23.8 ppm Co, 13.6 ppm Sc, and 286–293 ppm Zr. However, DR14-02, as well as DR18-01, which belong to Phase 3b and are slightly more primitive and similar to Phase 1 (DR10 and DR12). MgO, K_2O, TiO_2, and Ni contents of DR18-01 and DR14-02 samples range from 4.2–4.4 wt%, 2.4–2.5 wt%, 3.1–3.3 wt%, and 19–43.9 ppm, respectively. Co, Sc, and Zr contents vary between 26.3–27.6 ppm, 14.2–15.1 ppm, and 286–292 ppm, respectively.

Finally, the youngest flow also erupted during Phase 3b, DR20, displays the most primitive composition of the northwestern eruptive site with 4.5 wt% MgO, 2.3 wt% K_2O, 3.3 wt% TiO_2, 42.9 ppm Ni, 30.5 ppm Co, 13.8 ppm Sc, and 292 ppm Zr.

5.5. *Mineral chemistry*

The compositions of olivine crystals in Phase 1 samples (DR01, DR10, and DR12) approximate a Gaussian distribution with a Fo content varying from 70 to 73% (Figure 8 and Supplementary Table 2), suggesting the presence of a single population. Olivine crystals and the borders of reversely zoned olivine antecrysts in Phase 2 samples are slightly more evolved with a Fo content mainly below 71% (68–70% and 69–70% for DR08 and DR11, respectively, Figure 9). As described in previous work [e.g., Berthod et al., 2021b], the core of the zoned olivines have a much more evolved composition than the rims, ranging between $Fo_{56–57}$ and between $Fo_{52–60}$ in DR08 and DR11 samples, respectively. Phase 3a samples erupted at the northwestern site (DR14-01, DR14-03, DR15, and DR19) also contain two distinct populations of olivine: $Fo_{67–70}$ olivine crystals and zoned olivine antecrysts rims, which are more evolved than those from Phase 2, and $Fo_{56–63}$ cores of reversely zoned olivine (Figure 8). No olivine core has been analyzed in DR19 but they are visible in thin sections. The Fo content within the olivine crystals in Phase 3b samples vary from 69 to 72% (DR14-02, DR18-01, and DR20).

In all of our samples, Fe–Ti oxides in intergrowth with olivine crystals are Ti-rich magnetites, with FeO and TiO_2 contents ranging from 63.5 to 74.5 wt% and from 12.7 to 22.2 wt%, respectively (Supplementary Table 3). Magnetite-rimmed ilmenite observed in DR08, DR11, DR14, and DR15 samples are characterized by 45.5–50.7 wt% TiO_2, and 40.6–45.9 wt% FeO.

DR14-01, DR14-02, DR18-01, and DR20 samples contain plagioclase crystals with compositions at $An_{48–55}Ab_{42–48}Or_3$, $An_{51–58}Ab_{40–46}Or_{2–3}$, $An_{47–63}Ab_{35–49}Or_{2–4}$, and at $An_{53–58}Ab_{40–44}Or_{2–3}$ respectively (Supplementary Table 4).

Rare glassy melt inclusions are found in a variety of crystals (olivine, magnetite) and antecrysts (olivine, ilmenite, and magnetite) but are usually small (<10 μm). In order to identify the parent magma(s) of the antecryst cargo, we carefully looked for melt inclusions in antecrysts. We analyzed one larger inclusion in sample DR14-01, 70 μm in diameter and containing a gas bubble, hosted within the core of a reversely zoned olivine. The inclusion is tephri-phonolitic (56 wt% SiO_2 and 10 wt% $Na_2O + K_2O$) when normalized on an anhydrous basis, (Supplementary Table 5), and in equilibrium with its Fo_{60} olivine host [$Kd_{Fe/Mg}$ = 0.296 assuming 15% Fe^{3+} in the melt, Roeder and Emslie, 1970].

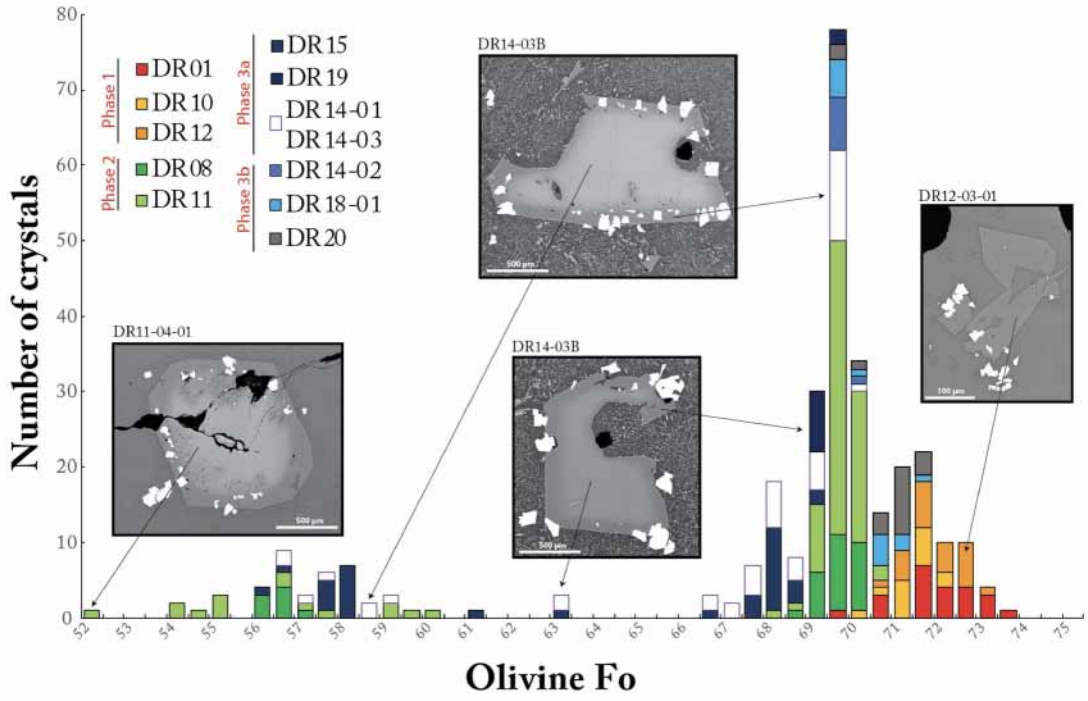

Figure 8. Histogram showing bimodal distribution of Fo content of analyzed olivine crystals from the eruption site. Most samples contain one single crystal population with Fo between 67 and 74%, but samples from Phase 2 and the early activity on the northwestern site contain a second population of more evolved olivine cores ($Fo_{52–63}$). Samples in the legend are presented in chronological order, from DR01, DR10, DR12 (Phase 1) to DR20 (Phase 3b, the latest erupted products, Figure 2).

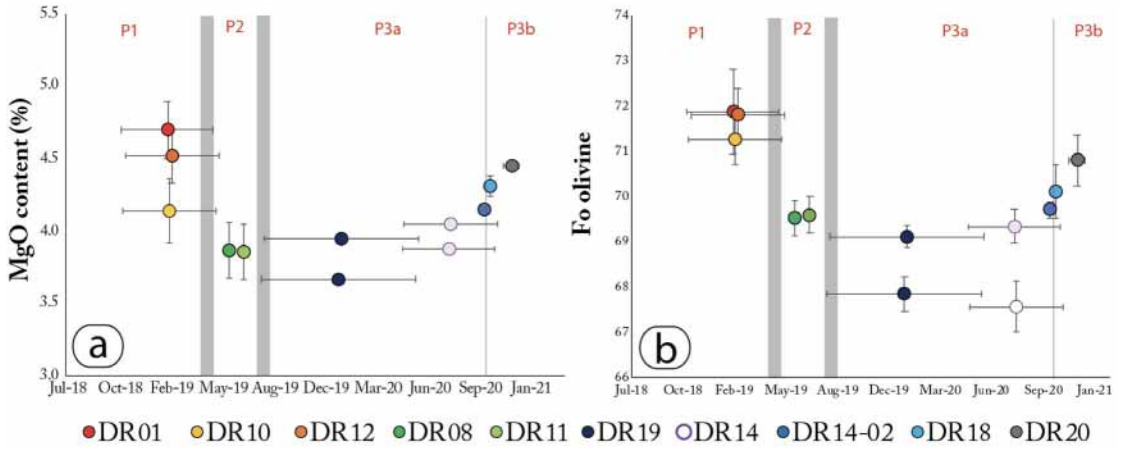

Figure 9. Geochemical evolution of the erupted products during the 2018–2021 eruption off the eastern coast of Mayotte. (A) Bulk-rock MgO content, (b) forsterite content in olivine crystals. Vertical error bars are two sigma standard deviations of the dataset for each sample. Uncertainties for the eruption times represent the possible time interval of the eruption, based on differential bathymetry during the various campaigns. P1–P3b: Phase 1 to Phase 3b.

6. Discussion

6.1. *Syn-eruptive evolution evidenced from high-precision sampling*

Following the methodology developed for subaerial eruptions at monitored volcanoes [Corsaro and Miraglia, 2005, 2022, Di Muro et al., 2014, Edmonds et al., 2013, Gansecki et al., 2019, Gurioli et al., 2018, Re et al., 2021], petrological and geochemical approaches provide an exceptional dataset for a submarine eruption sequence. Here, differential bathymetric datasets and high-precision dredging performed during the MAYOBS campaigns [Rinnert et al., 2019] allowed us to constrain the evolution of magma storage and transfer processes throughout this long-lived voluminous submarine eruption, both in time and space.

Phases 1 and 2 of the eruption were first sampled in May and July 2019, more than ten months after the beginning of the eruption, and when the Fani Maoré volcanic cone was already more than 800 m high. The samples, collected during the first three campaigns [MAYOBS 1, 2, and 4, Feuillet, 2019, Jorry, 2019, Fouquet and Feuillet, 2019, Rinnert et al., 2019], are therefore probably not representative of the very first lavas erupted during this eruption. Phase 1 lavas sampled by the DR01, DR10, and DR12 dredges are crystal-poor basanites (4.0–5.0 wt% MgO, Figure 7) with skeletal crystals (Figure 4a,b) and high pre-eruptive water content [up to 2.3 wt%, Berthod et al., 2021b]. During this first phase that spanned the first year of the eruption (Figure 2), the Fani Maoré eruption was fed by direct ascent of magma from a deep mantle lithospheric reservoir [≥35 km deep, Berthod et al., 2021b] to the surface. The shape and size of crystals (one single population with skeletal habits) indicate that most of the crystallization occurred late, in the shallow part of the ascending dyke. Phase 2 lavas (DR08 and DR11 samples, Figure 2) are more evolved (3.4 to 4.3 wt% MgO, Figure 7) than those from Phase 1. They contain reversely zoned olivine antecrysts ($Fo_{68–70}$ rims surrounding $Fo_{52–60}$ cores, Figures 4c–f and 8). Berthod et al. [2021b] showed that this magmatic evolution is mirrored by a decrease in vesicularity (from an average of 35 vol.% for phase 1 to 18 vol.% for phase 2), vesicle number density and dissolved water content, indicating that Phase 2 lavas were increasingly outgassed. Reverse zoning in olivine antecrysts records the interaction between the hot basanitic magma, ascending from ≥35 km, and more differentiated magma residing at shallower depths. Altogether, Phases 1 and 2 correspond to the eruption of ~5.0 km^3 of magma [Deplus et al., 2019, Feuillet et al., 2021].

Using samples collected during the MAYOBS 15 (DR14, DR15, and DR18, Table 1) and GEOFLAMME campaigns (DR19 and DR20, Table 1), we can now provide new petrological evidence on the eruptive sequence. As of August 2019, the eruption switched to a new site located 6 km northwest from the Fani Maoré volcanic edifice, i.e. more than 5 km from the lava flows dredged at the end of Phase 2, in July 2019, west of the main cone (DR11). There is no evidence that these two eruptive sites could have worked simultaneously, but this cannot be completely ruled out either. This change of the eruption site and the construction, at this new eruptive vent, of a large volcanic complex of more than 1.55 km^3 between August 2019 and January 2021 [REVOSIMA, 2020, 2022, Deplus et al., 2019], is the result of a significant shift in magma transfer during the eruption. This leads us to define a third phase for the eruptive sequence starting in August 2019. However, it is important to note that the first lava flows emplaced at this NW eruptive vent area (DR15 and DR19, Phase 3a) have similar compositions and mineral assemblages than the 2019 July distal flows (DR08 and DR11), with 3.6–3.7 wt% bulk MgO, $Fo_{67–69}$ olivine crystals, and zoned olivine antecrysts with $Fo_{56–63}$ cores (Figures 5, 7 and 8). Subsequent flows, emplaced between May and October 2020 (DR14-01 and DR14-03 samples, Figures 5, 7, and 8), also share the same characteristics. Phase 3a samples are thus similar to Phase 2 samples but emplaced at a different location.

On the contrary, later eruptive products emplaced at the end of 2020 within the northwestern eruptive area (Phase 3b, after October, Figure 2), are more primitive with whole-rock and mineral compositions and assemblages similar to the early products of Phase 1 (bulk-rock MgO up to 4.5 wt%, $Fo_{70–72}$ olivine, Figures 7 and 8, absence of reversely zoned olivine antecrysts, Figures 5 and 6). So, we consider that the samples from dredges DR18 and DR20 may characterize a new phase of the eruption or an evolution of the Phase 3.

To summarize, we observed a geochemical evolution of the eruptive products towards more evolved

composition until October 2020 (Figure 9). Eruptive products then became more primitive, reaching compositions approaching that of the early erupted products. Processes such as (1) fractional crystallization followed by a recharge of a more primitive composition, or (2) mixing with a more differentiated melt until exhaustion of this melt, can account for such geochemical evolution.

6.2. *Syn-eruption variations related to fractional crystallization*

Using whole-rock and mineral analyses, we showed a slight geochemical evolution within Phase 1 lavas (Figures 7–9). Bulk MgO content decreases from 4.4–5.0 wt%, 4.3–4.7 wt% to 4.0–4.2 wt% in DR01, DR12, and DR10 samples, respectively (Figures 7 and 9a). Olivine compositions follow the same trend with forsterite content slightly decreasing from 70–73%, 71–73% to 70–72% in DR01, DR12, and DR10 samples, respectively (Figures 8 and 9b).

These small, but significant, compositional variations contrast with the size of the very large 820 m-high Fani Maoré edifice built between July 2018 and May 2019 (Phase 1) during a complex evolution consisting of multiple constructional structures (Figure 2). The dimension of the eruptive area, which extends more than 10 km in latitude and 5 km in longitude, and the morphologies constituting the volcanic edifice (central lava cone, ridges that are probably rift zones, an extensive and well-developed lava tunnel system and distal flows) are consistent with the existence of multiple construction phases. It is important to note that the samples characterizing Phase 1 were collected on the flanks (near the summit and along the ridges) of the Fani Maoré volcanic edifice. They probably are compositions more representative of the end of the construction of this very large and voluminous volcanic cone of several km^3, given that the early products were completely buried and/or have not been sampled yet. The overall poorly evolved nature of Phase 1 magmas (44.2–46.3 wt% SiO_2 and low 4.0–5.0 wt% MgO, Figure 7), their temperature [1151 ± 20 °C; Berthod et al., 2021b], their aphyric and highly vesicular character, indicate a very low viscosity and confirms that Phase 1 lavas can spread over several kilometers.

The early development and growth of the Phase 1 and Phase 2 edifice may result from (i) multiple vents distributed with a N–S orientation and/or (ii) multiple pulses of magma arriving at the surface with different compositions in distinct sectors. It is likely, as frequently observed during high-eruption rate of voluminous Hawaiian basaltic eruptions [Gansecki et al., 2019], that the eruption started with numerous vents on a linear surface expression of the underlying feeding dyke with high-volume eruption rate and that progressively the activity concentrated to a more localized "cylindrical vent" in order to maintain thermal energy. Our petrological and geochemical data do not allow us to determine which process predominates. Whatever the development and growth of the edifice, our data shows that the slight geochemical evolution found in Phase 1 eruptive products is related to fractional crystallization of the magma in the deep magma reservoir [Berthod et al., 2021b]. Magma evolution of Phases 1 and 2 could be compatible with crystallization of clinopyroxene (decreasing CaO/Al_2O_3 and Sc with decreasing MgO, Figure 7c,f) and olivine (decreasing Ni, Co, Cr, and Cu with MgO, Figure 7c,d). A significant decrease in V and FeO may be related to magnetite fractionation although it could at least in part be explained by significant clinopyroxene fractionation. In both Phase 1 and Phase 2 products, there is no evidence of feldspar fractionation: Na_2O, K_2O, and Ba are strongly incompatible, and Eu concentrations show no anomaly [Berthod et al., 2021b]. In order to quantify this fractional crystallization hypothesis, we used both trace element and Rhyolite-MELTS models [Ghiorso and Sack, 1995, Gualda et al., 2012, Ghiorso and Gualda, 2015].

Using a back-crystallization model similar to the one developed by Späth et al. [1996], Berthod et al. [2021b] concluded that the most primitive basanite erupted by Fani Maoré is derived from primary mantle melts through deep fractionation of a cumulate composed of 80% clinopyroxene and 20% olivine. A similar forward model was computed by adding small increments of equilibrium olivine and clinopyroxene compositions, starting from the most primitive composition DR01-04 (Supplementary Table 1). The proportions of olivine and clinopyroxene were adjusted to fit the general trend of lavas from the eruption site (Figure 10, Supplementary Table 6). The entire trend from the eruption site could be explained by ~7% of crystallization (20% ol + 80% cpx). The fit is usually good, except for

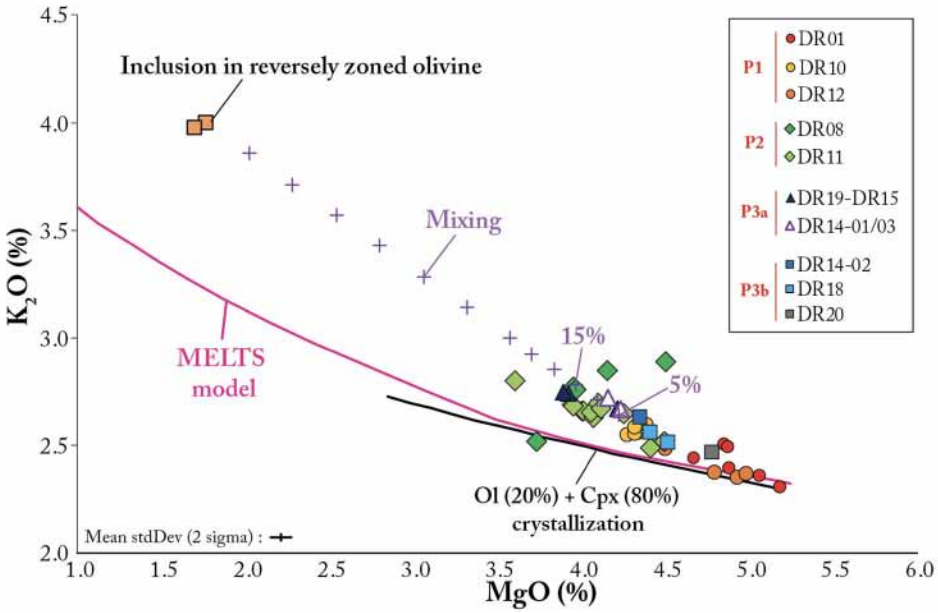

Figure 10. Fractional crystallization models (80% cpx and 20% ol crystallization model and Rhyolite-MELTS modeling at 1.0 GPa, FMQ-1, with 2.3 wt% H_2O) and mixing model performed to reproduce the syn-eruptive geochemical evolution trend. Our fractional crystallization models fit well with the trend of Phase 1 (DR01, DR10, and DR12). However, none of our fractional crystallization models can explain the rest of the eruptive sequence. We suggest that the geochemical signature of Phase 2 and Phase 3 lava flows is related to different amounts of magma tapping the differentiated subcrustal magma storage zone. Purple crosses represent the mixing line between sample DR10 (composition of the deep basanitic magma at the end of Phase 1) and the melt inclusion in reversely zoned olivine (composition of the tephri-phonolitic magma from the shallower reservoir). P1–P3b: Phase 1 to Phase 3b.

K_2O (and in smaller amounts Na_2O) which cannot be fitted by a crystallization model beyond samples from Phase 1. The model also slightly overestimates Ti and Fe, but this could easily be explained by adding small amounts of magnetite crystallization.

A fractional crystallization model was also run using the Rhyolite-MELTS software [Ghiorso and Sack, 1995, Gualda et al., 2012, Ghiorso and Gualda, 2015]. We also use the bulk composition of the most primitive sample, DR01-04, as parental melt. Magma storage conditions were set at 1.0 GPa with 2.3 wt% H_2O and an oxygen fugacity at FMQ-1. Temperature decreased from 1250 to 950 °C, with a 10 °C step. Since no orthopyroxene and garnet crystals were found in Comoros lavas, they were excluded from the crystallizing assemblage.

Except for P_2O_5, our modeling results match well for all major elements with the trend defined by the compositions erupted at the beginning of the sequence (Phase 1) and are consistent with an evolution dominated by fractional crystallization producing the slight variability of Phase 1 (Figure 10, Supplementary Table 7). The geochemical differences between DR01 and DR10 samples (Phase 1) can be attributed to 7–9% of fractional crystallization of a crystalline assemblage composed of clinopyroxene, spinel, Fe–Ti oxides, and apatite (Figure 10). This magma evolution by fractional crystallization during part of Phase 1 could reflect progressive cooling of the deep magma reservoir during the first year of the eruption. However, our model cannot account for the evolution of lava composition for the rest of the eruptive sequence (Phases 2 and 3). For example, the evolution of K_2O contents analyzed in lava flows of Phases 2 and 3 shows a clear contrast with the modeled K_2O contents (Figure 10), indicating that another process involving potassium enrichment of the magma must occur.

6.3. *Syn-eruptive variations related to mixing*

The presence of reversely zoned olivine and magnetite-rimmed ilmenite in distal lava flows emplaced on the western and southern flanks of the main volcanic cone (Phase 2, DR08 and DR11, Figure 2) and in early lava flows emplaced at the northwestern site (Phase 3, DR15 and DR19, Figure 2) indicates an interaction between the basanitic magma, and a shallower more evolved magma as shown by Berthod et al. [2021b]. Samples from Phase 2 and Phase 3 of the eruption are indeed aligned on a straight line between the later products of Phase 1 (DR10), and a potential composition for the shallower evolved magma, as represented by the composition of the glassy melt inclusions in equilibrium with the Fo_{59} and Fo_{57} cores of reversely zoned olivine (Figure 10).

To quantify the interaction between the two magmas, we use a simple mass balance model between sample DR10 (composition of the deep magma at the end of Phase 1) and the melt inclusions (composition of the evolved magma from the shallower reservoir). The core compositions of reversely zoned olivine antecrysts, although spanning a significant range (Fo contents from 52 to 63%, Figure 8) do not vary systematically during the eruption. The significant range could be explained by the sampling of a mush, and the absence of systematic variation suggests that the composition of the evolved magma varies little during the eruption. Also, reversely zoned olivine or magnetite-rimmed ilmenite represent less than 1% of the crystal cargo and have been only observed as isolated crystals (Figures 4 and 5) indicating that the magma ascending from the depths ≥35 km mainly sampled a melt with few crystals or efficiently dissolved them. We have therefore neglected the crystals in our model. Our results show that the percentage of magma sampled from the evolved shallower magma storage increased up to 14% of the volume released during the second year of the eruption, and then decreased from the beginning of 2020 (Figure 11).

From October 2020, magma composition became more primitive, and only a small percentage of evolved magma can be estimated for DR14-02, DR18-01, and DR20 samples (below standard deviations of the bulk-rock compositions). Evolution towards a more mafic magma during an eruption is usually interpreted as a recharge of the magma system by a more primitive and hotter magma [e.g., Moore et al., 2014]. However, we do not observe any evidence of mixing in crystal textures at the end of the eruption (Figure 6). Instead, we observed the disappearance of reversely zoned olivine or magnetite-rimmed ilmenite in those samples (DR18-01, DR20, and DR14-02, Figure 6) and the increase in the amount of $An_{47–63}Ab_{35–49}Or_{2–4}$ plagioclase in the matrix. This evolution during Phase 3b would rather be explained by a decrease in the amount of evolved magma assimilated by a higher volume of mafic intruded magma or by exhaustion of the mobilizable evolved magma stored in the shallower reservoir, or through a change in the magma ascent path.

Calculations, coupled with our petrological observations, suggest that the tephri-phonolitic shallower magma batch was sampled between May 2019 and mid-2020, and no longer during the last months of the eruption documented here. Using the DR14 samples (Figure 2), we can give a more precise date at which the sampling of this shallower magma batch stopped. Indeed, dredge DR14 sampled two distinct lava flows emplaced between May 2020 and October 2020 (DR14-01 and DR14-03 samples) and between October 6th and October 13th, 2020 (DR14-02 sample). DR14-01 and DR14-03 contain reversely zoned olivine and magnetite-rimmed ilmenite, whereas DR14-02 does not, which thus suggests that the tephri-phonolitic shallower magma storage was no longer sampled as of the beginning of October 2020.

6.4. *Magma ascent during the eruption*

We already have evidence of several changes in the dyke pathway during the eruption (Figure 12). Berthod et al. [2021b] suggested that the eruption of a more evolved magma in Phase 2 could have resulted from a change in a dyke pathway around May 2019. As of August, the eruption changed site and continued 6 km NW of the main central edifice leading us to propose the onset of a third phase. We note, however, that the compositions of the lava flows (Phase 3a, DR15 and DR19, Figure 7) are similar to Phase 2 with evolved lavas carrying reversely zoned olivine or magnetite-armored ilmenite (Figures 5 and 6). Therefore, the magma intrusion pathway change, or its northward extension, occurred in the crust above the shallower reservoir. The lack of change in the depth and location of the deep seismic swarm during

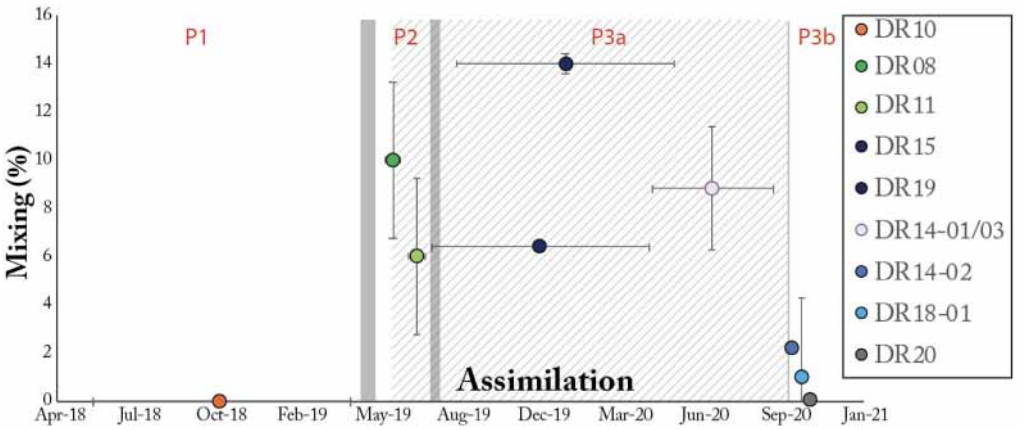

Figure 11. Average percentage of magma from the differentiated shallower magma storage in the erupted products calculated for each dredge. These estimates were obtained from a simple mass balance using the DR10 analyses for the deep magma composition. Estimated magma composition from the shallower reservoir was obtained from a glassy magmatic inclusion in the core of a reversely zoned olivine.

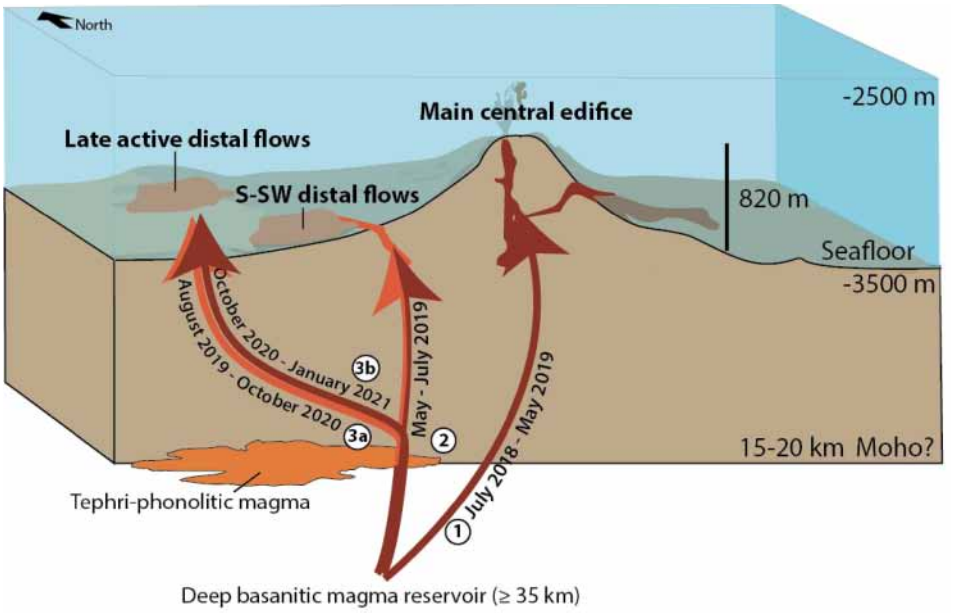

Figure 12. Diagram (not to scale) illustrating the dynamics of the magmatic plumbing system feeding the eruption. We propose to divide the eruption sequence into three distinct phases induced by two magma pathway changes. (Phase 1) During the first year of the eruption, the Fani Maoré eruption was fed by direct ascent of a basanitic magma from a deep mantle lithospheric reservoir [≥35 km deep, Berthod et al., 2021b] to the surface. (Phase 2) In May 2019, basanitic magma ascent slowed and switched to a pathway that sampled a shallower and tephri-phonolitic magma batch at the base of the crust [Berthod et al., 2021b]. (Phase 3a) In August 2019, the magma pathway shifted again in the crust resulting in a new eruption site located 6 km northwest of the main edifice. (Phase 3b) Finally, latest petrological and geochemical variations are associated with the exhaustion of the magma stored in the shallower reservoir.

the eruption is consistent with the hypothesis that the petrological variations of lavas, as well as the location of a new eruptive vent 6 km to the northwest of the main edifice, are caused by modifications of the physical properties associated with the more superficial magma reservoir and the crustal zone above it [Lavayssiere et al., 2022]. This change in a dyke pathway could also be related to the significant weight of the 820 m-high Fani Maoré volcanic edifice, which might have made it difficult for magma to rise vertically once the flow rate and overpressure decreased over time. Finally, a Phase 3b can be proposed from October 2020 until January 18, 2021 (the last evidence of new lava eruption at the time of writing in June 2022) with the end of the sampling of the shallower storage. The tephri-phonolitic magma storage has been sampled for almost a year and a half after (Figure 11). Petrological observations, coupled with mass-balance modeling, concluded that this shallow reservoir was no longer sampled as of October 2020. Reversely zoned olivine originating from the shallower reservoir display a Fo content varying from 52 to 63%, which does not change over time (Figure 7), suggesting that this reservoir was homogeneous in composition. A syn-eruptive magma path change is probably not the most likely scenario. In fact, we note that the regular and constant compositional evolution of the latest lavas can be explained by a decrease in the amount of evolved magma assimilated and finally by exhaustion of that evolved magma stored in the shallower reservoir. Therefore, we suggest that this change results from the complete emptying of the magma reservoir.

The petrological signature of the erupted magmas suggests that there are several magma storage zones containing eruptible melt beneath the Eastern Volcanic Chain of Mayotte (Figure 1b), but also that the high-flux eruption of large volumes of magma from a deep-seated reservoir below the Moho can influence and trigger the subsequent tapping of eruptible melt in the crust located at shallower depth just below the Moho [Berthod et al., 2021a]. This has implications with respect to the capacity of such large eruptions to reactivate shallow-seated zones of a large long-lasting magmatic system, which can feed continuing eruptive activity with magmas of different petrological characteristics and different volatile contents [Bachmann and Bergantz, 2004, Wark et al., 2007, Singer et al., 2016]. This conceptual model needs further validation and could be of paramount importance to assess the eruptive potential of the main polybaric magmatic system or mush system below the Horseshoe area of the Mayotte oriental submarine volcanic chain, located within 10 km of Petite Terre and 50 km of the Fani Maoré edifice (Figure 1b), which is probably one of the most active areas of the entire volcanic chain and is currently associated with most of the volcano-tectonic, long-period (LP), and very long-period (VLP) seismicity [Saurel et al., 2022, Retailleau et al., 2020, Lavayssiere et al., 2022] as well as fluid emissions rich in CO_2, methane, and H_2 [REVOSIMA bulletins; Mastin et al., 2022]. Furthermore, more detailed geomorphological and textural analysis need to be considered to constraint physical properties of the erupted material that controls the ascent dynamics and submarine emplacement.

7. Conclusion

With twenty-six oceanographic campaigns, the 2018–2021 Fani Maoré eruption off the coasts of Mayotte is the most intensively monitored submarine eruption. Time-lapsed bathymetric surveys coupled with high-precision submarine dredging allowed us to follow, for the first time, the syn-eruptive evolution of the magma at the submarine eruptive site. Our petrological and geochemical analyses carried out on the dredged lava flows provide an exceptional description of the evolution of the entire submarine eruption sequence that could be tracked and monitored at a regularly spaced interval from May 2019 to January 2021. Our observations enable us to divide the eruption sequence into three main different phases induced by two distinct magma pathway changes: (1) The first year of the eruption (Phase 1) is fed by direct ascent of a basanitic magma (4.0–5.0 wt% MgO) from the deep reservoir to the surface. (2) In May 2019, magma ascent slowed and switched to a pathway that sampled a tephri-phonolitic magma batch at the base of the crust (Phase 2); Lava flows display evidence of assimilation (reversely zoned olivine) and a more evolved composition (3.4–4.3 wt% MgO). (3) Three months later, the activity shifted to a new eruptive area 6 km northwest of the main edifice, Fani Maoré, starting a third phase. Since the Phase 3a lava flows are similar to Phase 2, we suggest that the magma pathway switched again in the crust after the sampling of the tephri-phonolitic magma batch.

Finally, a third evolution is defined in October 2020, associated with the exhaustion of the magma stored in the shallower reservoir (Phase 3b) and a return to compositions similar to Phase 1. From petrological models (crystallization and mass-balance models), we proposed that the initial geochemical evolution (Phase 1) can be explained by 7–9% of fractional crystallization at 1.0 GPa with 2.3 wt% H_2O and an oxygen fugacity at FMQ-1 from the most primitive samples. However, fractional crystallization cannot explain the rest of the eruptive sequence (Phases 2 and 3) and we suggest that the geochemical signature of Phases 2 and 3 is related to mixing with an older differentiated subcrustal magma storage.

These new data help determine the dynamics of the magmatic systems feeding the remarkable Fani Maoré eruption and provide critical constraints on the shallow magma ascent pathway (<20 km) which cannot be imaged geophysically since no seismic signals are recorded at these depths.

Conflicts of interest

Authors have no conflict of interest to declare.

Acknowledgements

MAYOBS 1 campaign was funded by the CNRS-INSU TELLUS MAYOTTE program (SISMAYOTTE project). MAYOBS 1, 2, 4, and 15 campaigns were conducted by several French research institutions and laboratories (IPGP/CNRS/BRGM/IFREMER/IPGS). All marine operations are performed as part of the MAYOBS set of campaigns (https://doi.org/10.18142/291) and we thank the captains and crews of the R/V Marion Dufresne (TAAF/IFREMER/LDA), R/V Pourquoi Pas? (GENAVIR/IFREMER, SHOM), R/V Beautemps-Beaupré (SHOM), and R/V Gauss (FUGRO). The GEOFLAMME oceanographic campaign (CNFH; PI C. Cathalot, E. Rinnert, N. Feuillet) also funded marine operations that benefited to this study and provided dredge samples. Analyses were funded by the Service National d'Observation en Volcanologie (SNOV, INSU) and the Réseau de Surveillance Volcanologique et Sismologique de Mayotte (REVOSIMA), a partnership between the Institut de Physique du Globe de Paris (IPGP), the Bureau de Recherches Géologiques et Minières (BRGM), the Observatoire Volcanologique du Piton de la Fournaise (OVPF-IPGP), the Centre National de la Recherche Scientifique (CNRS), and the Institut Français de Recherche pour l'Exploitation de la Mer (IFREMER). Since June 2019, all activities on Mayotte are funded by the Ministère de l'Enseignement Supérieur, de la Recherche et de l'Innovation (MESRI), the Ministère de la Transition Ecologique (MTE), the Ministère des Outremers (MOM), the Ministère de l'Intérieur (MI), and the Ministère des Armées, with the support of the Direction Interministérielle aux Risques Majeurs en Outremer (DIRMOM) and the Mission d'Appui aux Politiques Publiques pour la Prévention des Risques Majeurs en Outremer (MAPPPROM). The authors would like to thank E. Humler for his support and national funding coordination (CNRS, REVOSIMA). Finally, we are also grateful for the helpful reviews provided by the Guest Editors Vincent Famin and Jerome van der Woerd, by Helène Balcone Boissard and an anonymous reviewer. This study contributes to IdEx Université de Paris ANR-18-IDEX-0001. Trace element analyses were supported by IPGP multidisciplinary program PARI and by Paris–IdF region SESAME Grant no. 12015908. This project has received funding from the European Union's Horizon 2020 research and innovation programme under grant agreement no. 731070. This is Labex ClerVolc contribution number 567.

Supplementary data

Supporting information for this article is available on the journal's website under https://doi.org/10.5802/crgeos.155 or from the author.

Appendix A. Protocol for sorting and describing samples

Prior to the arrival of the dredge on deck, special care was taken to clean the deck and to ensure that no sample remained from previous dredges to avoid contamination. When the dredge was above deck, it was turned over and emptied. Whenever the dredge contained popping rocks, it was shaken then put "at rest" on deck for a few hours for safety reasons.

An initial description of the contents of the dredge was performed, and pictures of the bulk products were taken, both within the dredge and with the rocks on the deck. These pictures can help to

approximately position the first collected samples (at the base of the dredge) and the last ones (at the top).

As soon as we could approach the newly-dredged material, samples were sorted into different lithological and textural categories or types. For instance, for volcanic rocks, categories can be fresh/juvenile, altered and non-juvenile materials. If the juvenile material was effusive, lava fragments were divided according to their typology: whole or fragment (glassy rim, interior) of pillow (see Section 4.2), lava sheet (crust, interior), lava tunnel roof, and column. Descriptions included the vesicle size, density, and morphology (rounded, elongated, pipes), crystal content, crystal nature and size, as well as the presence of enclaves (mingling, xenoliths, cumulates), iron-rich surficial deposits (crust), traces of gas sublimates and/or /hydrothermal mineralization, and datable organic material. Pyroclastic fragments (bombs, lapilli, ashes) were distinguished from their texture (glassy, dense, vesiculated), and their size or coloration. Everything that arguably predates the eruption, that had an altered appearance or had a different color, such as brecciated pyroclastic deposits, hemipelagic sedimentary deposits, organic material, and crystal-rich fragments were considered as non-juvenile to even non volcanic fragments.

After this classification was completed, each sample was then described with a magnifying glass and a binocular microscope, to refine and complete the separation in different lithological types and their description.

The second description step consisted in taking pictures of the selected samples with a scale, a label and a sample number. A consistent numbering scheme has been defined for each campaign off the coasts of Mayotte Mayotte. For instance, for the monitoring survey MAYOBS 15 campaign, the following numbering has been set: MAY15 (campaign number)—DR14 (dredge number) 01 (family number) 01 (subclass number if necessary). To follow standard regulation an International Geo Sample Number (IGSN) had to be given before storage in sample depositaries at Ifremer and IPGP/Chambon.

In general, two boxes (about 30 kg each) were kept as archives in the sample depositaries of IFREMER and IPGP to be available for analytical work and sample requests from the scientific community. An additional 2–3 boxes, based on weight or selected samples for dedicated investigations, were also kept for each participating institution involved in the systematic petrological monitoring. A selection of smaller most important samples including fresh glass were brought back in the airplane by the participating scientists in order to perform rapid geochemical analyses and in some cases geochronological measurements. The bulk of the archived material returns via marine shipping along with the equipment. Unfortunately, not all samples can be brought back, and after careful study on board, samples from the MAYOBS campaigns that are not selected (usually we keep about 200–300 kg of rocks) are stored onboard in a crate that will be emptied at the end of the campaign during transit at the same specific site that is well outside the studied area and well identified in the logbook for future reference (Start: 16°50.40 S, 52°37.67 E; End: 16°51.70 S, 52°38.54 E).

References

Bachèlery, P., Gurioli, L., Berthod, C., Komorowski, J.-C., Peltier, A., Saurel, J.-M., Lemarchand, A., and REVOSIMA Consortium (2021). European catalogue of volcanoes. UCA-OPGC and IPGP. Retrieved from https://volcanos.eurovolc.eu/?volcano=MAY#.

Bachèlery, P. and Hémond, C. (2016). Geochemical and petrological aspects of Karthala volcano. In Bachèlery, P., Lénat, J.-F., Di Muro, A., and Michon, L., editors, *Active Volcanoes of the Southwest Indian Ocean: Piton de la Fournaise and Karthala. Active Volcanoes of the World*, pages 367–384. Springer-Verlag, Berlin and Heidelberg. Chap. 23.

Bachèlery, P., Morin, J., Villeneuve, N., Soulé, H., Nassor, H., and Ali, A. R. (2016). Structure and eruptive history of Karthala volcano. In Bachèlery, P., Lénat, J.-F., Di Muro, A., and Michon, L., editors, *Active Volcanoes of the Southwest Indian Ocean: Piton de la Fournaise and Karthala. Active Volcanoes of the World*, pages 345–366. Springer-Verlag, Berlin and Heidelberg. Chap. 22.

Bachmann, O. and Bergantz, G. W. (2004). On the origin of crystal-poor rhyolites: Extracted from batholithic crystal mushes. *J. Petrol.*, 45(8), 1565–1582.

Bamber, E. C., Arzilli, F., Polacci, M., Hartley, M. E., Fellowes, J., Di Genova, D., Chavarria, D., Armando Ceballos, J., and Burton, M. R. (2020).

Pre-and syn-eruptive conditions of a basaltic Plinian eruption at Masaya Volcano, Nicaragua: the Masaya Triple Layer (2.1 ka). *J. Volcanol. Geotherm. Res.*, 392, article no. 106761.

Berthod, C., Médard, E., Bachèlery, P., Gurioli, L., Di Muro, A., Peltier, A., Komorowski, J.-C., Benbakkar, M., Devidal, J.-L., Langlade, J., Besson, P., Boudon, G., Rose-Koga, E., Deplus, C., Le Friant, A., Bickert, M., Nowak, S., Thinon, I., Burckel, P., Hidalgo, S., Kaliwoda, M., Jorry, S., Fouquet, Y., and Feuillet, N. (2021a). The 2018-ongoing Mayotte submarine eruption: Magma migration imaged by petrological monitoring. *Earth Planet. Sci. Lett.*, 571, article no. 117085.

Berthod, C., Médard, E., Di Muro, A., Hassen Ali, T., Gurioli, L., Chauvel, C., Komorowski, J.-C., Benbakkar, M., Devidal, J.-L., Besson, P., Le Friant, A., Deplus, C., Nowak, S., Thinon, I., Burckel, P., Hidalgo, S., Feuillet, N., Jorry, S., and Fouquet, Y. (2021b). Mantle xenolith-bearing phonolites and basanites feed the active volcanic ridge of Mayotte (Comoros archipelago, SW Indian Ocean). *Contrib. Mineral. Petrol.*, 176(10), 1–24.

Berthod, C., Zaragosi, S., and Famin, V. (2021c). SCRATCH cruise. RV Marion Dufresne.

Bertil, D., Mercury, N., Doubre, C., Lemoine, A., and Van der Woerd, J. (2021). The unexpected Mayotte 2018–2020 seismic sequence: a reappraisal of the regional seismicity of the Comoros. *C. R. Géosci.*, 353(S1), 211–235.

Bertil, D. and Regnoult, J. M. (1998). Seismotectonics of Madagascar. *Tectonophysics*, 294, 57–74.

Carey, R., Soule, S. A., Manga, M., White, J. D. L., McPhie, J., Wysoczanski, R., Jutzeler, M., Tani, K., Yoerger, D., Fornari, D., Caratori-Tontini, F., Houghton, B., Mitchell, S., Ikegami, F., Conway, C., Murch, A., Fauria, K., Jones, M., Cahalan, R., and McKenzie, W. (2018). The largest deep-oceansilicic volcanic eruption of the past century. *Sci. Adv.*, 4, article no. e1701121.

Casas, D., Pimentel, A., Pacheco, J., Martorelli, E., Sposato, A., Ercilla, G., et al. (2018). Serreta 1998–2001 submarine volcanic eruption, offshore terceira (azores): Characterization of the vent and inferences about the eruptive dynamics. *J. Volcanol. Geotherm. Res.*, 356, 127–140.

Cesca, S., Letort, J., Razafindrakoto, H. N. T., Heimann, S., Rivalta, E., Isken, M. P., Nikkhoo, M., Passarelli, L., Petersen, G. M., Cotton, F., and Dahm, T. (2020). Drainage of a deep magma reservoir near Mayotte inferred from seismicity and deformation. *Nat. Geosci.*, 13, 87–93.

Clague, D. A., Paduan, J. B., Dreyer, B. M., Chadwick Jr, W. W., Rubin, K. R., Perfit, M. R., and Fundis, A. T. (2018). Chemical variations in the 1998, 2011, and 2015 lava flows from Axial Seamount, Juan de Fuca Ridge: Cooling during ascent, lateral transport, and flow. *Geochem. Geophys. Geosyst.*, 19, 2915–2933.

Class, C., Goldstein, S. L., Altherr, R., and Bachèlery, P. (1998). The process of plume–lithosphere interactions in the ocean basins—the case of Grande Comore. *J. Petrol.*, 39, 881–903.

Claude-Ivanaj, C., Bourdon, B., and Allègre, C. J. (1998). Ra–Th–Sr isotope systematics in Grande Comore Island: a case study of plume–lithosphere interaction. *Earth Planet. Sci. Lett.*, 164, 99–117.

Corsaro, R. A. and Miraglia, L. (2005). Dynamics of 2004–2005 Mt. Etna effusive eruption as inferred from petrologic monitoring. *Geophys. Res. Lett.*, 32, article no. L13302.

Corsaro, R. A. and Miraglia, L. (2022). Near real-time petrologic monitoring on volcanic glass to infer magmatic processes during the February–April 2021 Paroxysms of the South-East Crater, Etna. *Front. Earth Sci.*, 10, article no. 828026.

Deniel, C. (1998). Geochemical and isotopic (Sr, Nd, Pb) evidence for plume–lithosphere interactions in the genesis of Grande Comore magmas (Indian Ocean). *Chem. Geol.*, 144, 281–303.

Deplus, C., Feuillet, N., Bachelery, P., Fouquet, Y., Jorry, S., Thinon, I., Bermell, S., Besson, F., Gaillot, A., Guérin, C., Le Friant, A., Paquet, F., Pierre, D., and Pitel-Roudaut, M. (2019). Early development tand growth of a deep seafloor volcano: Preliminary results from the MAYOBS cruises. In *Abstract V43I-0227, 2019 Fall Meeting*. AGU, San Francisco.

Di Muro, A., Métrich, N., Vergani, D., Rosi, M., Armienti, P., Fougeroux, T., Deloule, E., Arienzo, I., and Civetta, L. (2014). The shallow plumbing system of Piton de la Fournaise Volcano (La Réunion Island, Indian Ocean) revealed by the major 2007 caldera forming eruption. *J. Petrol.*, 55, 1287–1315.

Edmonds, M., Sides, I. R., Swanson, D. A., Werner, C., Martin, R. S., Mather, T. A., Herd, R. A., Jones, R. L., Mead, M. I., and Sawyer, G. (2013). Magma storage, transport and degassing during the 2008–10 summit eruption at Kilauea Volcano, Hawai'i. *Geochim. Cosmochim. Acta*, 123, 284–301.

Famin, V., Michon, L., and Bourhane, A. (2020). The Comoros archipelago: a right-lateral transform boundary between the Somalia and Lwandle plates. *Tectonophysics*, 789, article no. 228539.

Feuillet, N. (2019). MAYOBS1 cruise. RV Marion Dufresne.

Feuillet, N., Jorry, S., Crawford, W., Deplus, C., Thinon, I., Jacques, E., Saurel, J.-M., Lemoine, A., Paquet, F., Satriano, C., Aiken, C., Foix, O., Kowalski, P., Laurent, A., Rinnert, E., Cathalot, C., Donval, J. P., Guyader, V., Gaillot, A., Scalabrin, C., Moreira, M., Peltier, A., Beauducel, F., Grandin, R., Ballu, V., Daniel, R., Pelleau, P., Gomez, J., Besançon, S., Géli, L., Bernard, P., Bachèlery, P., Fouquet, Y., Bertil, D., Lemarchand, A., and Van Der Woerd, J. (2021). Birth of a large volcanic edifice offshore Mayotte via lithosphere-scale dyke intrusion. *Nat. Geosci.*, 14(10), 787–795.

Foix, O., Aiken, C., Saurel, J. M., Feuillet, N., Jorry, S. J., Rinnert, E., and Thinon, I. (2021). Offshore Mayotte volcanic plumbing revealed by local passive tomography. *J. Volcanol. Geotherm. Res.*, 420, article no. 107395.

Fouquet, Y. and Feuillet, N. (2019). MAYOBS4 cruise. RV Marion Dufresne.

Gansecki, C., Lee, R. L., Shea, T., Lundblad, S. P., Hon, K., and Parcheta, C. (2019). The tangled tale of Kīlauea's 2018 eruption as told by geochemical monitoring. *Science*, 366, article no. eaaz0147.

Ghiorso, M. S. and Gualda, G. A. (2015). An H2O-CO2 mixed fluid saturation model compatible with rhyolite-MELTS. *Contrib. Mineral. Petrol.*, 169, 1–30.

Ghiorso, M. S. and Sack, R. O. (1995). Chemical mass transfer in magmatic processes IV. A revised and internally consistent thermodynamic model for the interpolation and extrapolation of liquid–solid equilibria in magmatic systems at elevated temperatures and pressures. *Contrib. Mineral. Petrol.*, 119, 197–212.

Gualda, G. A., Ghiorso, M. S., Lemons, R. V., and Carley, T. L. (2012). Rhyolite-MELTS: a modified calibration of MELTS optimized for silica-rich, fluid-bearing magmatic systems. *J. Petrol.*, 53, 875–890.

Gurioli, L., Di Muro, A., Vlastélic, I., Moune, S., Thivet, S., Valer, M., Villeneuve, N., Boudoire, G., Peltier, A., and Bachèlery, P. (2018). Integrating field, textural, and geo-chemical monitoring to track eruption triggers and dynamics: a case study from Piton de la Fournaise. *Solid Earth*, 9, 431–455.

Gurioli, L., Houghton, B. F., Cashman, K. V., and Cioni, R. (2005). Complex changes in eruption dynamics and the transition between Plinian and phreatomagmatic activity during the 79 AD eruption of Vesuvius. *Bull. Volcanol.*, 67, 144–159.

Jochum, K. P., Weis, U., Schwager, B., Stoll, B., Wilson, S. A., Haug, G. H., Andreae, M. O., and Enzweiler, J. (2016). Reference values following ISO guidelines for frequently requested rock reference materials. *Geostand. Geoanal. Res.*, 40, 333–350.

Jorry, S. J. (2019). MAYOBS2 cruise. RV Marion Dufresne.

Kidd, R. B., Huggett, Q. J., and Ramsay, A. T. S. (1990). The status of geological dredging techniques. *Mar. Geol. Surv. Sampl.*, 12, 131–143.

Lavayssiere, A., Crawford, W. C., Saurel, J.-M., Satriano, C., Feuillet, N., Jacques, E., and Komorowski, J.-C. (2022). A new 1d velocity model and absolute locations image the Mayotte seismo-volcanic region. *J. Volcanol. Geotherm. Res.*, 421, article no. 107440.

Lemoine, A., Briole, P., Bertil, D., Roullé, A., Foumel, M., Thinon, I., Raucoules, D., de Michele, M., and Valty, P. (2020). The 2018–2019 seismo-volcanic crisis east of Mayotte, Comoros islands: seismicity and ground deformation markers of an exceptional submarine eruption. *Geophys. J. Int.*, 223(1), 22–44.

Liu, E. J., Cashman, K. V., Miller, E., Moore, H., Edmonds, M., Kunz, B. E., Jenner, F., and Chigna, G. (2020). Petrologic monitoring at Volcán de Fuego, Guatemala. *J. Volcanol. Geotherm. Res.*, 405, article no. 107044.

Magee, R., Ubide, T., and Caulfield, J. (2021). Days to weeks of syn-eruptive magma interaction: High-resolution geochemistry of the 2002–03 branched eruption at Mount Etna. *Earth Planet. Sci. Lett.*, 565, article no. 116904.

Masquelet, C., Leroy, S., Delescluse, M., Chamot-Rooke, N., Thinon, I., Lemoine, A., Franke, D., Watremez, L., Werner, P., Paquet, F., Berthod, C., Cabiativa, V., and Sauter, D. (2022). The East-Mayotte new volcano in the Comoros archipelago: structure and timing of magmatic phases inferred from seismic reflection data. *C. R. Géosci.*, 354(S2), 65–79.

Mastin, M., Cathalot, C., Rouxel, O., Gaucher, E. C., Donval, J. P., Guyader, V., Germain, Y., Scalabrin, C., Jouenne, S., Dehez, S., and Rinnert, E. (2022). Strong geochemical anomalies following active

submarine eruption offshore Mayotte. In *Ocean Sciences Meeting 2022, DS08 The Impact of Submarine Hydrothermal and Volcanic Activity on Ocean Chemistry and Biology 03. 24 February–4 March 2022*. ASLO, Waco, TX.

Moore, A., Coogan, L. A., Costa, F., and Perfit, M. R. (2014). Primitive melt replenishment and crystal-mush disaggregation in the weeks preceding the 2005–2006 eruption 9 50′ N, EPR. *Earth Planet. Sci. Lett.*, 403, 15–26.

Morin, J., Bachèlery, P., Soule, H., and Nassor, H. (2016). Volcanic risk and crisis management on Grande Comore island. In Bachèlery, P., Lénat, J.-F., Di Muro, A., and Michon, L., editors, *Active Volcanoes of the Southwest Indian Ocean: Piton de la Fournaise and Karthala. Active Volcanoes of the World*, pages 403–422. Springer-Verlag, Berlin and Heidelberg. Chap. 25.

Nougier, J., Cantagrel, J. M., and Karche, J. P. (1986). The Comores archipelago in the Western Indian Ocean: Volcanology, geochronology and geodynamic setting. *J. Afr. Earth Sci. (1983)*, 5(2), 135–144.

Pelleter, A. A., Caroff, M., Cordier, C., Bachèlery, P., Nehlig, P., Debeuf, D., and Arnaud, N. (2014). Melilite-bearing lavas in Mayotte (France): An insight into the mantle source below the Comores. *Lithos*, 208, 281–297.

Piochi, M., Mastrolorenzo, G., and Pappalardo, L. (2005). Magma ascent and eruptive processes from textural and compositional features of Monte Nuovo pyroclastic products, Campi Flegrei, Italy. *Bull. Volcanol.*, 67, 663–678.

Quidelleur, X., Michon, L., Famin, V., Geffray, M. C., Danišík, M., Gardiner, N., Rusquet, A., and Zakaria, M. G. (2022). Holocene volcanic activity in Anjouan Island (Comoros archipelago) revealed by new Cassignol-Gillot groundmass K–Ar and ^{14}C ages. *Quat. Geochronol.*, 67, article no. 101236.

Re, G., Corsaro, R. A., D'Oriano, C., and Pompilio, M. (2021). Petrological monitoring of active volcanoes: A review of existing procedures to achieve best practices and operative protocols during eruptions. *J. Volcanol. Geotherm. Res.*, 419, article no. 107365.

Resing, J. A., Rubin, K. H., Embley, R. W., Lupton, J. E., Baker, E. T., Dziak, R. P., et al. (2011). Active submarine eruption of boninite in the northeastern Lau Basin. *Nat. Geosci.*, 4, 799–806.

Retailleau, L., Saurel, J.-M., Issartel, S., Zhu, W., Beroza, G. C., Satriano, C., Ferrazzini, V., and Komorowski, J.-C. (2020). Automatic detection of the seismicity associated to the Maytte volcanic crisis. In *Fall Meeting 2020*. American Geophysical Union, Washington, DC. Abstract #V040-0002.

Reubi, O., Blundy, J., and Pickles, J. (2019). Petrological monitoring of Volcán de Colima magmatic system: the 1998 to 2011 activity. In *Volcán de Colima*, pages 219–240. Springer, Berlin, Heidelberg.

REVOSIMA (2019). Bulletin n°2 du 1 au 15 août 2019, Bulletin bi-mensuel de l'activité sismo-volcanique à Mayotte. IPGP, Université de Paris, OVPF, BRGM, Ifremer, CNRS, January, 6th, 2021, http://www.ipgp.fr/revosima, http://www.ipgp.fr/sites/default/files/ipgp_1er_bulletin_info_sismo_volcanique_mayotte-cor.pdf.

REVOSIMA (2020). Bulletin n°24 de l'activité sismo-volcanique à Mayotte. IPGP, Université de Paris, OVPF, BRGM, Ifremer, CNRS, January, 6th, 2021, http://www.ipgp.fr/revosima, http://www.ipgp.fr/sites/default/files/ipgp_revosima_n24_08122020.pdf.

REVOSIMA (2022). Bulletin n°38 de l'activité sismo-volcanique à Mayotte. 1 au 31 janvier 2022, IPGP, Université de Paris, OVPF, BRGM, Ifremer, CNRS, 4 février 2022, http://www.ipgp.fr/revosima, http://www.ipgp.fr/sites/default/files/ipgp_revosima_n38_20220204.pdf.

Rinnert, E., Cathalot, C., and Feuillet, N. (2021). GEOFLAMME cruise. RV Pourquoi Pas?

Rinnert, E., Feuillet, N., Fouquet, Y., Jorry, S., Thinon, I., and Lebas, E. (2019). MD 228/MAYOBS.

Rinnert, E., Thinon, I., and Feuillet, N. (2020). MD 228/MAYOBS15 cruise. RV Marion Dufresne, https://doi.org/10.17600/18001745.

Roeder, P. L. and Emslie, R. F. (1970). Olivine-liquid equilibrium. *Contrib. Mineral. Petrol.*, 29, 275–289.

Saurel, J. M., Jacques, E., Aiken, C., Lemoine, A., Retailleau, L., Lavayssiere, A., Foix, A., Dofal, A., Laurent, A., Mercury, N., Crawford, W., Lemarchand, A., Daniel, R., Pelleau, P., Bes de Berc, M., Dectot, G., Bertil, D., Roullé, A., Broucker, C., Colombain, A., Besancon, S., Guyavarch, P., Kowalski, P., Roudaut, M., Battaglia, J., Bodihar, S., Bouin, M. P., Canjamale, K., Desfete, N., Doubre, C., Dretzen, R., Ferrazzini, V., Fontaine, F., Geli, L., Griot, C., Grunberg, M., Can Guzel, E., Hoste-Colomer, R., Lambotte, S., Leger, F., Vergnes, J., Satriano, C., Tronel,

F., Van der Woerd, J., Feuillet, N., Fouquet, Y., Jorry, S. J., Rinnert, E., and Thinon, I. (2022). Mayotte seismic crisis: building knowledge in near real-time by combining land and ocean-bottom seismometers, first results. *Geophys. J. Int.*, 228(2), 1281–1293. Publisher's official version: https://doi.org/10.1093/gji/ggab392. Open Access version: https://archimer.ifremer.fr/doc/00724/83604/.

Singer, B. S., Costa, F., Herrin, J. S., Hildreth, W., and Fierstein, J. (2016). The timing of compositionally-zoned magma reservoirs and mafic "priming" weeks before the 1912 Novarupta-Katmai rhyolite eruption. *Earth Planet. Sci. Lett.*, 451, 125–137.

Späth, A., Roex, A. P. L., and Duncan, R. A. (1996). The geochemistry of lavas from the Comores Archipelago, Western Indian Ocean: petrogenesis and mantle source region characteristics. *J. Petrol.*, 37, 961–991.

Stamps, D. S., Kreemer, C., Fernandes, R., Rajaonarison, T. A., and Rambolamanana, G. (2021). Redefining East African rift system kinematics. *Geology*, 49(2), 150–155.

Sundermeyer, C., Di Muro, A., Gordeychick, B., and Wörner, G. (2020). Timescales of magmatic processes during the eruptive cycle 2014–2015 at Piton de la Fournaise, La Réunion, obtained from Mg-Fe diffusion modelling in olivine. *Contrib. Mineral. Petrol.*, 175, 1–16.

Thinon, I., Lemoine, A., Leroy, S., Paquet, F., Famin, V., Feuillet, N., Berthod, C., Doubre, C., Jacques, E., Zaragosi, S., Clouard, V., Bernard, J., Delescluse, M., Franke, D., Jorry, S. J., Van der Woerd, J., Watremez, L., Boymond, P., Masquelet, C., Rusquet, A., Mercury, N., Roche, V., Bachèlery, P., Sauter, D., Michon, L., Chamot-Rooke, N., Rolandone, F., Scalabrin, C., Deplus, C., Rad, S., Bujan, S., Dassie, E., Bignon, J., Canva, A., Sitti allaouia, S., Ali, S., Morvan, L., Hardouin, E., and Sadeski, L. (2022). Volcanism and tectonics unveiled between the EARS and Madagascar: toward a better understanding of the geodynamics of the Comoros archipelago. *C. R. Géosci.*, 354(S2), 7–34.

Thinon, I., Leroy, S., and Lemoine, A. (2021). SISMAORE cruise. RV Pourquoi Pas?

Thivet, S., Carlier, J., Gurioli, L., Di Muro, A., Besson, P., Smietana, M., Boudon, G., Bachelery, P., Eychenne, J., and Nedelec, J.-M. (2022). Magmatic and phreatomagmatic contributions on the ash-dominated basaltic eruptions: insights from the April and November–December 2005 eruptions at Karthala volcano, Comoros. *J. Volcanol. Geotherm. Res.*, 424, article no. 107500.

Thivet, S., Gurioli, L., and Di Muro, A. (2020). Basaltic dyke eruptions at Piton de La Fournaise: characterization of the eruptive products with implications for reservoir conditions, conduit processes and eruptive dynamics. *Contrib. Mineral. Petrol.*, 175, article no. 26.

Tzevahirtzian, A., Zaragosi, S., Bachèlery, P., Biscara, L., and Marchès, E. (2021). Submarine morphology of the Comoros volcanic archipelago. *Mar. Geol.*, 432, article no. 106383.

Wark, D. A., Hildreth, W., Spear, F. S., Cherniak, D. J., and Watson, E. B. (2007). Pre-eruption recharge of the Bishop magma system. *Geology*, 35(3), 235–238.

Zinke, J., Reijmer, J. J. G., Thomassin, B. A., Dullo, W. C., Grootes, P. M., and Erlenkeuser, H. (2003). Postglacial flooding history of Mayotte lagoon (Comoro archipelago, southwest Indian Ocean). *Mar. Geol.*, 194(3–4), 181–196.